Editors' Suggestion | Featured in Physics

Active Optical Intensity Interferometry

Lu-Chuan Liu,[1,2,3] Cheng Wu,[1,2,3] Wei Li,[1,2,3] Yu-Ao Chen,[1,2,3] Xiao-Peng Shao,[4] Frank Wilczek,[5,6,7,8,9,†] Feihu Xu,[1,2,3] Qiang Zhang,[1,2,3,*] and Jian-Wei Pan[1,2,3,‡]

[1]*Hefei National Research Center for Physical Sciences at the Microscale and School of Physical Sciences, University of Science and Technology of China, Hefei, 230026, China*
[2]*Shanghai Research Center for Quantum Science and CAS Center for Excellence in Quantum Information and Quantum Physics, University of Science and Technology of China, Shanghai, 201315, China*
[3]*Hefei National Laboratory, University of Science and Technology of China, Hefei, 230026, China*
[4]*Xi'an Institute of Optics and Precision Mechanics of CAS, Xi'an 710119, China*
[5]*Center for Theoretical Physics, MIT, Cambridge, Massachusetts 02139, USA*
[6]*T. D. Lee Institute, Shanghai Jiao Tong University, Shanghai, 200240, China*
[7]*Wilczek Quantum Center, School of Physics and Astronomy, Shanghai Jiao Tong University, Shanghai, 200240, China*
[8]*Department of Physics, Stockholm University, Stockholm, SE-106 91, Sweden*
[9]*Department of Physics, Arizona State University, Tempe, Arizona 85287, USA*

(Received 28 September 2024; revised 6 April 2025; accepted 10 April 2025; published 9 May 2025)

Long baseline diffraction-limited optical aperture synthesis technology by interferometry plays an important role in scientific study and practical application. In contrast to amplitude (phase) interferometry, intensity interferometry—which exploits the second-order coherence of thermal light—is robust against atmospheric turbulence and optical defects. However, a thermal light source typically has a broadband spectrum, a low average photon number per mode, and a wide divergence angle, forestalling extended applications. Here, we propose and demonstrate active intensity interferometry for optical synthetic aperture imaging over the kilometer range. Our scheme employs multiple phase-independent laser emitters to generate thermal illumination and utilizes a flexible computational algorithm for image reconstruction. Through outdoor experiments, we have successfully imaged millimeter-scale targets located at 1.36 km away, achieving a resolution enhancement by about 14 times over the diffraction limit of a single telescope. The application of long-baseline active intensity interferometry holds promise for advancing high-resolution optical imaging and sensing.

DOI: 10.1103/PhysRevLett.134.180201

Introduction—Hanbury Brown and Twiss (HBT) first proposed the seminal idea of high-angle resolution intensity interferometry for the measurement of stellar diameter [1–3], which is a technique based on the measurement of temporal correlations of arrival time between photons recorded in different detectors. The intensity interferometry does not require a high-precision phase stabilization system, and it is robust against optical imperfections and atmospheric turbulence [4]. Hence, it is much easier to implement than amplitude (phase) interferometry. In astrophysics, the forthcoming air Cherenkov telescope arrays, which consist of almost 100 telescopes, are the current largest optical intensity interference project [5,6]. Following its start in astronomy, intensity interferometry has been developed as a versatile lab tool in general research fields, including the probe of interactions in high-energy particle physics [7], studying the photon propagation in nonlinear media [8] and curved space [9], measurements of quantum correlations in ultracold bosonic and fermionic systems [10–12], and identification of single photon sources [13].

Although intensity interferometry has been well studied in passive imaging scenes [14,15], it remains rarely explored in the field of active imaging, i.e., light detection and ranging (LiDAR). Benefiting from flexible active illumination schemes, LiDAR has emerged as a powerful tool to image non-self-luminous targets [16,17]. In passive imaging applications, intensity interferometry is hard to achieve because the imaging targets of interest are typically black body sources (e.g., stars) with a low average photon number per mode [18]. In contrast, active intensity interferometry can exploit thermal illumination with a higher average photon number per mode to improve the measurement signal-to-noise ratio (SNR). To probe high resolution and resist atmospheric turbulence, active intensity interferometry has emerged as a great candidate. However, the lack of collimated narrow-spectrum thermal

*Contact author: qiangzh@ustc.edu.cn
†Contact author: wilczek@mit.edu
‡Contact author: pan@ustc.edu.cn

illumination schemes and robust imaging retrieval algorithms imposes practical difficulties for its applications in active synthetic aperture imaging.

Intensity interference characterizes the second-order coherence of thermal light. It can also be interpreted as the photon bunching effect in a quantum framework [3,19], and the shape of the bunching peak in spatial domain is squared proportional to the Fourier transform of the shape of the source [20,21]. In experiments, intensity interference is obtained by cross-correlating intensity fluctuations measured in different pairs of telescopes to achieve aperture synthesis and yield resolution enhancement. In general, unlike lasers, thermal light sources cannot simultaneously meet the requirements of intense light power, narrow spectra, and small divergence angles. A better alternative solution involves utilizing a composite approach integrating a laser source with a spatial-temporal modulation device, such as a rotating ground glass [22–25], a spatial light modulator [26], and a projector [27] to synthesize a pseudothermal light source. Laboratory intensity interferometry has demonstrated imaging of simple targets, such as simulated binary stars formed by randomly scattered lasers [28,29]. However, these pseudothermal light sources are incompetent for long-range active illumination due to their large divergence angle, typically exceeding 100 mrad for off-the-shelf diffusers.

In this Letter, we show that a phase-independent multiple laser emitter array can act as a pseudothermal light source (divergence angle < 1 mrad), satisfying both the thermal nature of the source and the requirement of long-range illumination for intensity-interferometry imaging. In the experiment, we illuminate the targets with eight independent laser emitters modulated by the atmosphere and receive the back-reflected photons using two telescopes with configurable transverse range. For image retrieval, we develop an elaborate data preprocessing technique equipped with a modified phase retrieval algorithm, each tailored to adapt the active intensity interferometric data. Together, we experimentally realize optical synthetic aperture imaging over 1.36 km in an outdoor urban environment. The imaging resolution is about 3 mm, which is about 14 times enhancement over the diffraction limit of a single telescope of 42.5 mm. The experimental results embrace our extended intensity interferometry theory.

Theory—Optical intensity interferometry typically necessitates that the imaging target to be a thermal light source to measure the non-shot-noise-induced intensity variations on two light detectors and compute their correlation. For ideal monochromatic polarized thermal light, Hanbury Brown and Twiss showed that the second-order intensity correlation function is proportional to the square of the modulus of the Fourier transform of the intensity distribution on the target surface. Mathematically, suppose we have two light detectors D_a and D_b, whose intensities measured at time t are $I_a(t)$ and $I_b(t)$, respectively, and let $\mathbf{k}_a$ and $\mathbf{k}_b$ be the wave vectors from the target to the detectors D_a and D_b, respectively. Then, according to the intensity interferometry theory [3], the normalized intensity correlation function $c_{ab}^{(2)}$ can be expressed as

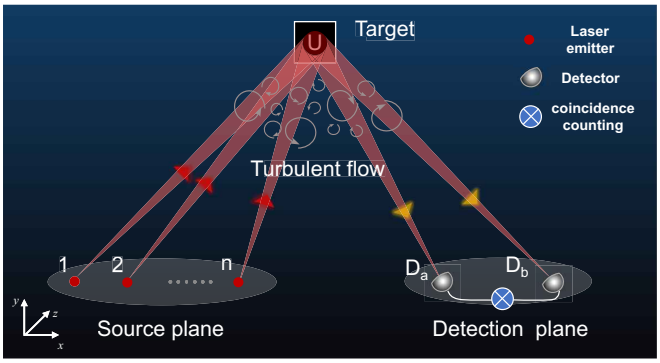

FIG. 1. Active optical intensity interferometry schematic. An active optical intensity interferometer comprises a source plane and a detection plane. The source plane features n laser emitters, originating from a single source and split into n beams by beam splitters, creating an n-way illumination directed at the target. Atmospheric turbulence randomly modulates each beam's phase, resulting in pseudothermal illumination. The target is oriented toward the source plane. The detection plane includes two movable detectors, D_a and D_b, which are used to measure $c_{ab}^{(2)}$ across different baselines.

$$c_{ab}^{(2)} = \frac{\langle \Delta I_a(t) \Delta I_b(t) \rangle}{\langle I_a(t) \rangle \langle I_b(t) \rangle} = |f(\mathbf{k}_a - \mathbf{k}_b)|^2, \tag{1}$$

where $\langle \ldots \rangle$ is the time averaged notation, $\Delta I(t) \equiv I(t) - \langle I(t) \rangle$ and f is the normalized Fourier function of the target surface intensity distribution $\rho(\mathbf{r})$; that is,

$$f(\Delta\mathbf{k}) = \frac{\int \rho(\mathbf{r}) e^{-i\Delta\mathbf{k}\cdot\mathbf{r}} d\mathbf{r}}{\int \rho(\mathbf{r}) d\mathbf{r}}. \tag{2}$$

Let L be the distance from the target to the interferometer and λ be the wavelength of light. Since $\Delta\mathbf{k}$ and the projected interferometer baseline $\mathbf{B}$ have a proportional relationship that is $\Delta\mathbf{k} = 2\pi\mathbf{B}/(\lambda L)$, synthetic aperture can be achieved by changing $\mathbf{B}$ to cover a sufficiently large area of the u-v plane to obtain enough information about the target in the Fourier domain. The angular resolution of the intensity interferometer is about $\lambda/B_{\max}$ at the wavelength λ, which is larger than that of a single telescope [3].

However, when intensity interferometry is used for active imaging, it is hard to illuminate distant targets with poorly collimated thermal light sources. On the other hand, if we illuminate the target with well-collimated coherent light, such as a laser, intensity interference cannot be observed because light detectors can only measure the

intensity signal fluctuations induced by shot noise, which are uncorrelated with each other.

To overcome the above difficulties, a basic idea is to superimpose a collection of phase-independent coherent lights to achieve pseudothermal illumination. As illustrated in Fig. 1, for simple verification, we eliminate the requirement for phase modulators by utilizing atmospheric turbulence to randomly modulate the phases of multiple laser emitters. In the case of such nonideal pseudothermal illumination, specklelike noise occurs when measuring the intensity correlation function, so we propose a statistical optics theory [see Supplemental Material (SM) Sec. H [30]], in which Eq. (1) needs to be modified to a form of the ensemble average, namely,

$$\langle c_{ab}^{(2)} \rangle_e = c_0 + c_1 |f(\mathbf{k}_a - \mathbf{k}_b)|^2, \tag{3}$$

where c_0 and c_1 are the coefficients jointly determined by the light intensity, the autocorrelation coefficient of different emitters, and the optical memory effect [44,45]. If we ignore the optical memory effect and consider a case where all laser emitters are symmetrically equivalent, then $c_0 = c/n$ and $c_1 = (n-1+c)/n$ are simple functions of the number of laser emitters n and the autocorrelation coefficient c.

The above statistical relationship allows us to extract information about the target in the Fourier domain from the measurement of the intensity correlation function. Specifically, considering that the ensemble average expression predicts the average result of multiple parallel measurements, for a single-shot measurement of $c_{ab}^{(2)}$, we can write $c_{ab}^{(2)} = \langle c_{ab}^{(2)} \rangle_e + \epsilon$, where ϵ is a random variable which denotes the speckle-like noise term that we wish to suppress as much as possible. We calculate an expression for the noise intensity (i.e., the standard deviation of $c_{ab}^{(2)}$) and find that it decreases to 0 at a rate of $O(1/\sqrt{n})$ as the number of laser emitters n increases (see SM, Sec. H [30]). This means that one way to suppress the experimental noise is to increase the number of laser emitters so that they are physically closer to thermal illumination. We also discuss the boundary cases of single ($n = 1$) and infinite ($n = \infty$) laser emitters, and show that the former will lead to a very low SNR, while the latter will give predictions that are consistent with classical HBT theory based on ideal thermal light sources.

Experimental setup—We implement an intensity interferometry imaging experiment in an urban atmospheric environment. Figure 2 shows an aerial view of the experiment setup, with the active intensity interferometer placed at location S, facing the imaging target located at T over a distance of 1.36 km (determined by laser ranging measurement). The active optical intensity interferometer consists of a phase-independent multiple laser emitter array and two identical receiving systems, as shown in Fig. 2(a).

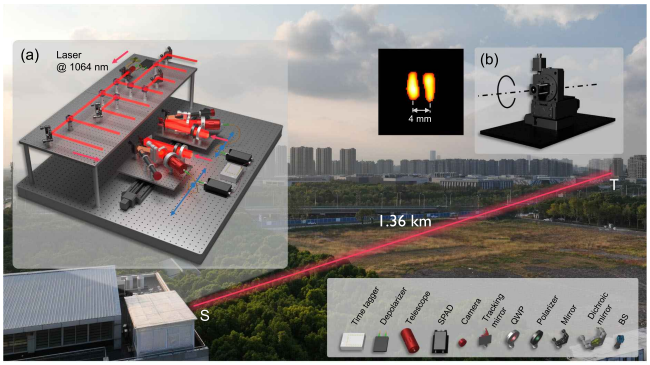

FIG. 2. Experimental setup: aerial diagram of a 1.36-km free-space link with an active intensity interferometer (S) and imaging target (T). (a) Active intensity interferometer: comprising a continuous-wave (CW) laser emitter array and two identical receiving systems. The emitter array, utilizing beam splitters (BSs) and reflectors, splits the depolarized light into eight beams, each directed towards the imaging target. Receiving systems, mounted on translation stages, collect left circularly polarized light through a quarter-wave plate (QWP) and a linear polarizer. A dichroic mirror spectrally separates the light: signal portion collected by telescope to single-photon avalanche diode (SPAD), background to camera for tracking. Photon arrival times recorded by time-to-digital converter (TDC). (b) Imaging target: mounted on motorized rotation stage. (Inset) Double slit imaging result.

The target is put on the three-axis motorized rotation stages, as shown in Fig. 2(b).

In the laser emitter array, a 1064 nm CW laser (∼100 mW) is depolarized by a single-mode optical fiber depolarizer. Depolarized illumination can reduce the intensity fluctuation caused by different polarization reflectivities of the target. The depolarized light is then coupled into free space by a collimator with a focal length of 40 mm and is divided into eight beams with equal spatial separation and power by a group of BSs. Eight beams are adjusted to point at the target, and the beam radius expands to ∼0.2 m after propagating 1.36 km, larger than the size of the target. The distance between two adjacent laser emitter is fixed to 0.15 m, larger than the outer scale of atmospheric turbulence (the atmospheric coherence length typically measured 0.02–0.05 m), to ensure that each beam has an independent random phase shift [46,47]. In the theoretical analysis, we prove that a collection of phase-independent multiple coherent light can be equivalent to a pseudothermal light source.

Two identical receiving systems, D_a and D_b, are separately placed on two linear translation stages to change the baseline from 0.07 m to 0.87 m per 0.04 m steps. To achieve sufficient 2D baseline coverage, when the baseline is set to a specific length, the target is rotated every 6° in the range of 0–360°. The receiving system collects circularly polarized light through a QWP and a linear polarizer to avoid intensity fluctuations caused by polarization changes during target rotation. A tracking mirror mounted on a

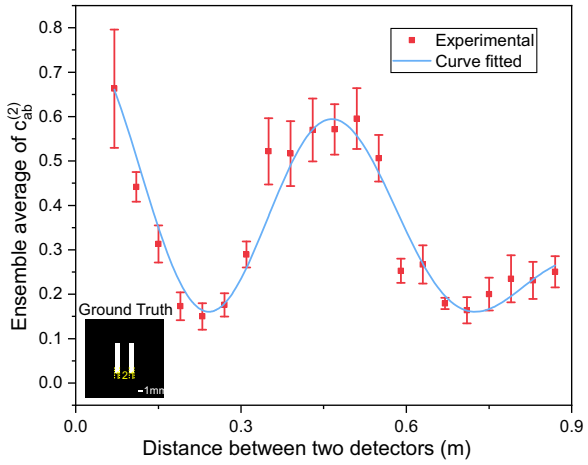

FIG. 3. Ensemble averaged $c_{ab}^{(2)}$ measurements of a double slit in the horizon direction. In the horizon direction, the two slits are both 1 mm wide, and the center distance between the two slits is 3 mm. We assume the spatial ergodicity of speckle [48] and use the average of the $c_{ab}^{(2)}$ measurements corresponding to 100 random minor changes in the target attitude as an ensemble average measurement (red dot). The blue curve is the least squares fitting result of Eq. (3) with fitting parameters $c_0 = 0.160$ and $c_1 = 0.625$.

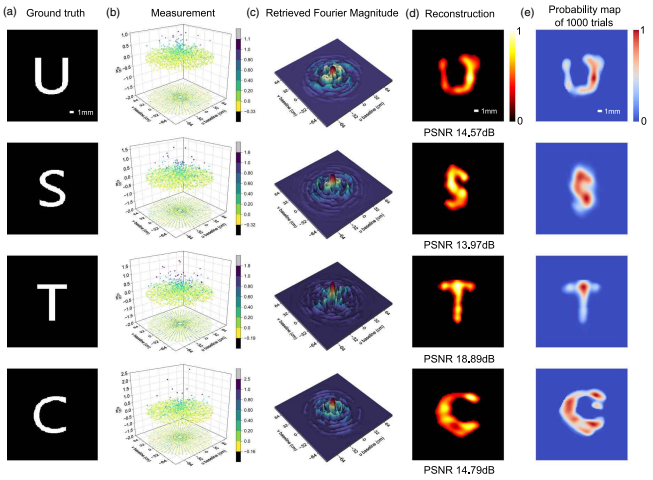

FIG. 4. Main experimental results. (a) Ground truth targets. (b) Raw measurements of $c_{ab}^{(2)}$ at a distance of 1.36 km for targets listed in (a). Colored dots with 2D x-y projection mark the observed 1260 sparse data points. (c) Retrieved Fourier magnitude from (b) via data preprocessing. (d) Reconstructed target images from (c) using the proposed phase retrieval algorithm. (e) Probability map with 1000 independent phase retrieval trials. Scale bars: 1 mm (a),(d),(e).

piezo platform is used for closed-loop tracking, ensuring that the target remains within the field of view while the receiving system moves. A dichroic mirror is introduced to separate the collected light spectrally. Using a telescope with a diameter of 42.5 mm and a focal length of 80 mm, the 1064 nm signal light transmitted through the dichroic mirror is coupled to a 62.5-μm multimode optical fiber and then guided to a silicon SPAD. Other background light is reflected by the dichroic mirror and enters a camera with a 300 mm focal length lens for feedback on the tracking mirror pointing.

The arrival time information of photons at two SPADs is recorded using a TDC, from which $c_{ab}^{(2)}$ can be measured. The time bin and integration time of coincidence counting measurements are set to 2 ms and 2 s, respectively. The imaging targets are made of retroreflective sheetings covered with blackened aluminum plates hollowed out into various patterns, making the reflective areas about 10 mm^2. The count rate of each SPAD is about 10^4 Hz and the coincidence measurement SNR is about 10 (see SM, Secs. H and I, for more details [30]).

Result—We first demonstrate the effectiveness of the proposed framework by observing a double slit. As shown in Fig. 3, Eq. (3) is verified by the ensemble average measurement of $c_{ab}^{(2)}$ and the result shows that an image with a 3 mm cross-range resolution at 1.36 km can be achieved. The theoretical resolution predicted by the Rayleigh diffraction limit is $1.22\lambda L/B_{\max} \approx 2.03$ mm, where λ, L, and $B_{\max}$ represent the illumination wavelength, the imaging distance, and the maximum size of the synthetic aperture, respectively. Similarly, the diffraction limit of a 42.5 mm diameter telescope is calculated to be 41.5 mm, so our system achieves a resolution enhancement of a single receiving aperture by a factor of 41.5 mm/3 mm ≈ 14.

Then we perform synthetic aperture imaging on the letter targets [Fig. 4(a)]. The size of each letter is 8 mm by 9 mm, with 1.5 mm in thickness. According to our experimental setup, a total of $60 \times 21 = 1260$ $c_{ab}^{(2)}$ data points measured over a limited area on the u-v plane are rebinned to conform to a frequels with a 512×512 frequel grid [Fig. 4(b)]. To recover real-space image pixels from Fourier space signals, the phase of the Fourier transform must be determined in addition to its magnitude [49–51]. After applying an elaborated preprocessing pipeline to the $c_{ab}^{(2)}$ raw measurements, we retrieve the targets' Fourier magnitude [Fig. 4(c)], enabling a modified phase retrieval algorithm to reconstruct two-dimensional target images. The relevant computational retrieval method is given in detail in SM, Sec. B [30]. Reconstruction results with peak signal-to-noise ratio (PSNR) of 14–19 dB demonstrate the feasibility of the proposed method [Fig. 4(d)]. A superposition of 1000 individual trials of phase retrieval results is shown in Fig. 4(e), which clearly demonstrates moderate image restoration fidelity and stability. Potential image quality improvement may be achieved by increasing the number of laser emitters n, the capture frames as well as the sampling ratio in the interferometric plane (SM, Secs. C and E–G [30]). Further imaging comparisons with direct telescope observations can be found in SM, Sec. D [30].

Discussion—In summary, we have proposed an extended framework of active optical intensity interferometry and experimentally demonstrated synthetic aperture imaging over the kilometer range. In the experiment, phase-independent multiple laser emitters based on the phase fluctuations of atmosphere turbulence can act as an elegant pseudothermal light source to illuminate long-range objects, but the modulation speed is limited to atmospheric coherence time. With the introduction of an active phase modulation scheme and a confocal receiving-emitting telescope array, high-speed active intensity interferometry imaging is an interesting avenue for future work. On the other hand, higher-fidelity reconstruction is anticipated by applying more advanced methods, such as the optimization strategy and deep learning modules. In the future, efforts can be devoted to jointly measure the first and second-order coherence of light to uncover improved imaging resolution. Further integrating the active intensity interferometry with deep space exploration and microscopy will facilitate high-resolution imaging from macroscopic scale to microscopic scale.

Acknowledgments—We thank Zhen-Tao Liu and Shen-Sheng Han from the Shanghai Institute of Optics and Fine Mechanics for their suggestions on this work. This research was supported by the National Natural Science Foundation of China (Grants No. T2125010, No. 62031024, and No. 12204466); Innovation Programme for Quantum Science and Technology (Grants No. 2021ZD0300100 and No. 2021ZD0300303); Natural Science Foundation of Shanghai (Grant No. 22ZR1468200); Anhui Initiative in Quantum Information Technologies (Grant No. AHY010100); and Shanghai Municipal Science and Technology Major Project (Grant No. 2019SHZDZX01). Y.-A. C., F.-H. X., and Q. Z. were supported by the New Cornerstone Science Foundation through the Xplorer Prize. F. W. was supported by the U.S. Department of Energy under grant Contract No. DE-SC0012567, by the European Research Council under Grant No. 742104, and by the Swedish Research Council under Contract No. 335-2014-7424.

L.-C. L., C. W., and W. L. contributed equally to this work.

[1] R. H. Brown and R. Twiss, A test of a new type of stellar interferometer on Sirius, Nature (London) **178**, 1046 (1956).

[2] R. H. Brown and R. Q. Twiss, Interferometry of the intensity fluctuations in light-i. basic theory: The correlation between photons in coherent beams of radiation, Proc. R. Soc. A **242**, 300 (1957).

[3] R. H. Brown, *The Intensity Interferometer; Its Application to Astronomy* (Taylor & Francis, London; Halsted Press, New York, 1974).

[4] T. A. Smith and Y. Shih, Turbulence-free double-slit interferometer, Phys. Rev. Lett. **120**, 063606 (2018).

[5] M. Actis, G. Agnetta, F. Aharonian, A. Akhperjanian, J. Aleksić, E. Aliu, D. Allan, I. Allekotte, F. Antico *et al.* (The CTA Consortium), Design concepts for the cherenkov telescope array CTA: An advanced facility for ground-based high-energy gamma-ray astronomy, Exp. Astron. **32**, 193 (2011).

[6] A. Abeysekara, W. Benbow, A. Brill, J. Buckley, J. Christiansen, A. Chromey, M. Daniel, J. Davis, A. Falcone, Q. Feng *et al.*, Demonstration of stellar intensity interferometry with the four veritas telescopes, Nat. Astron. **4**, 1164 (2020).

[7] D. H. Boal, C.-K. Gelbke, and B. K. Jennings, Intensity interferometry in subatomic physics, Rev. Mod. Phys. **62**, 553 (1990).

[8] Y. Bromberg, Y. Lahini, E. Small, and Y. Silberberg, Hanbury brown and twiss interferometry with interacting photons, Nat. Photonics **4**, 721 (2010).

[9] V. H. Schultheiss, S. Batz, and U. Peschel, Hanbury brown and twiss measurements in curved space, Nat. Photonics **10**, 106 (2016).

[10] M. Henny, S. Oberholzer, C. Strunk, T. Heinzel, K. Ensslin, M. Holland, and C. Schönenberger, The fermionic Hanbury Brown and Twiss experiment, Science **284**, 296 (1999).

[11] T. Jeltes, J. M. McNamara, W. Hogervorst, W. Vassen, V. Krachmalnicoff, M. Schellekens, A. Perrin, H. Chang, D. Boiron, A. Aspect *et al.*, Comparison of the Hanbury Brown–Twiss effect for bosons and fermions, Nature (London) **445**, 402 (2007).

[12] R. Dall, A. Manning, S. Hodgman, W. RuGway, K. V. Kheruntsyan, and A. Truscott, Ideal n-body correlations with massive particles, Nat. Phys. **9**, 341 (2013).

[13] M. D. Eisaman, J. Fan, A. Migdall, and S. V. Polyakov, Invited review article: Single-photon sources and detectors, Rev. Sci. Instrum. **82**, 071101 (2011).

[14] D. Dravins, S. LeBohec, H. Jensen, and P. D. Nuñez, Stellar intensity interferometry: Prospects for sub-milliarcsecond optical imaging, New Astron. Rev. **56**, 143 (2012).

[15] V. Malvimat, O. Wucknitz, and P. Saha, Intensity interferometry with more than two detectors?, Mon. Not. R. Astron. Soc. **437**, 798 (2014).

[16] B. Behroozpour, P. A. Sandborn, M. C. Wu, and B. E. Boser, Lidar system architectures and circuits, IEEE Commun. Mag. **55**, 135 (2017).

[17] J. Rapp, J. Tachella, Y. Altmann, S. McLaughlin, and V. K. Goyal, Advances in single-photon lidar for autonomous vehicles: Working principles challenges, and recent advances, IEEE Signal Process. Mag. **37**, 62 (2020).

[18] M. Bojer, Z. Huang, S. Karl, S. Richter, P. Kok, and J. von Zanthier, A quantitative comparison of amplitude versus intensity interferometry for astronomy, New J. Phys. **24**, 043026 (2022).

[19] R. J. Glauber, Photon correlations, Phys. Rev. Lett. **10**, 84 (1963).

[20] P. H. Van Cittert, Die wahrscheinliche schwingungsverteilung in einer von einer lichtquelle direkt oder mittels einer linse beleuchteten ebene, Physica **1**, 201 (1934).
[21] F. Zernike, The concept of degree of coherence and its application to optical problems, Physica **5**, 785 (1938).
[22] G. Scarcelli, A. Valencia, and Y. Shih, Experimental study of the momentum correlation of a pseudothermal field in the photon-counting regime, Phys. Rev. A **70**, 051802(R) (2004).
[23] A. Valencia, G. Scarcelli, M. D'Angelo, and Y. Shih, Two-photon imaging with thermal light, Phys. Rev. Lett. **94**, 063601 (2005).
[24] F. Ferri, D. Magatti, A. Gatti, M. Bache, E. Brambilla, and L. A. Lugiato, High-resolution ghost image and ghost diffraction experiments with thermal light, Phys. Rev. Lett. **94**, 183602 (2005).
[25] O. Katz, P. Heidmann, M. Fink, and S. Gigan, Non-invasive single-shot imaging through scattering layers and around corners via speckle correlations, Nat. Photonics **8**, 784 (2014).
[26] J. H. Shapiro, Computational ghost imaging, Phys. Rev. A **78**, 061802(R) (2008).
[27] B. Sun, M. P. Edgar, R. Bowman, L. E. Vittert, S. Welsh, A. Bowman, and M. J. Padgett, 3d computational imaging with single-pixel detectors, Science **340**, 844 (2013).
[28] D. Dravins, T. Lagadec, and P. D. Nuñez, Long-baseline optical intensity interferometry-laboratory demonstration of diffraction-limited imaging, Astron. Astrophys. **580**, A99 (2015).
[29] D. Dravins, T. Lagadec, and P. D. Nuñez, Optical aperture synthesis with electronically connected telescopes, Nat. Commun. **6**, 6852 (2015).
[30] See Supplemental Material at http://link.aps.org/supplemental/10.1103/PhysRevLett.134.180201, which includes Refs. [31–43], for detailed derivations, as well as additional theoretical, numerical and experimental results.
[31] G. Ramachandran and A. Lakshminarayanan, Three-dimensional reconstruction from radiographs and electron micrographs: Application of convolutions instead of fourier transforms, Proc. Natl. Acad. Sci. U.S.A. **68**, 2236 (1971).
[32] J. R. Fienup, Reconstruction of an object from the modulus of its fourier transform, Opt. Lett. **3**, 27 (1978).
[33] J. Fienup and C. Wackerman, Phase-retrieval stagnation problems and solutions, J. Opt. Soc. Am. A **3**, 1897 (1986).
[34] S. Marchesini, Invited article: A unified evaluation of iterative projection algorithms for phase retrieval, Rev. Sci. Instrum. **78**, 011301 (2007).
[35] S. Marchesini, H. He, H. N. Chapman, S. P. Hau-Riege, A. Noy, M. R. Howells, U. Weierstall, and J. C. Spence, X-ray image reconstruction from a diffraction pattern alone, Phys. Rev. B **68**, 140101(R) (2003).
[36] D. F. Buscher, Simulating large atmospheric phase screens using a Woofer-Tweeter algorithm, Opt. Express **24**, 23566 (2016).
[37] A. Levi and H. Stark, Image restoration by the method of generalized projections with application to restoration from magnitude, J. Opt. Soc. Am. A **1**, 932 (1984).
[38] H. H. Bauschke, P. L. Combettes, and D. R. Luke, Hybrid projection–reflection method for phase retrieval, J. Opt. Soc. Am. A **20**, 1025 (2003).
[39] C. W. Beenakker, Random-matrix theory of quantum transport, Rev. Mod. Phys. **69**, 731 (1997).
[40] S. M. Popoff, G. Lerosey, R. Carminati, M. Fink, A. C. Boccara, and S. Gigan, Measuring the transmission matrix in optics: An approach to the study and control of light propagation in disordered media, Phys. Rev. Lett. **104**, 100601 (2010).
[41] J. W. Goodman, *Speckle Phenomena in Optics: Theory and Applications* (Roberts and Company Publishers, Greenwood Village, CO, 2007).
[42] I. Reed, On a moment theorem for complex Gaussian processes, IRE Trans. Inf. Theory **8**, 194 (1962).
[43] J. W. Goodman, *Statistical Optics* (John Wiley & Sons, New York, 2015).
[44] S. Feng, C. Kane, P. A. Lee, and A. D. Stone, Correlations and fluctuations of coherent wave transmission through disordered media, Phys. Rev. Lett. **61**, 834 (1988).
[45] I. Freund, M. Rosenbluh, and S. Feng, Memory effects in propagation of optical waves through disordered media, Phys. Rev. Lett. **61**, 2328 (1988).
[46] D. L. Fried, Optical resolution through a randomly inhomogeneous medium for very long and very short exposures, J. Opt. Sos. Am. A **56**, 1372 (1966).
[47] K. D. Ridley, Measurements of laser phase fluctuations induced by atmospheric turbulence over 2 km and 17.5 km distances, Appl. Opt. **50**, 5085 (2011).
[48] I. Freund, Looking through walls and around corners, Physica (Amsterdam) **168A**, 49 (1990).
[49] R. W. Gerchberg, A practical algorithm for the determination of plane from image and diffraction pictures, Optik (Stuttgart) **35**, 237 (1972), https://cir.nii.ac.jp/crid/1572261550522209664.
[50] J. R. Fienup, Phase retrieval algorithms: A personal tour, Appl. Opt. **52**, 45 (2013).
[51] Y. Shechtman, Y. C. Eldar, O. Cohen, H. N. Chapman, J. Miao, and M. Segev, Phase retrieval with application to optical imaging: A contemporary overview, IEEE Signal Process. Mag. **32**, 87 (2015).

Supplemental Material for Active Optical Intensity Interferometry

Lu-Chuan Liu,[1,2,3] Cheng Wu,[1,2,3] Wei Li,[1,2,3] Yu-Ao Chen,[1,2,3] Xiao-Peng Shao,[4] Frank Wilczek,[5,6,7,8,9] Feihu Xu,[1,2,3] Qiang Zhang,[1,2,3] and Jian-Wei Pan[1,2,3]

[1]*Hefei National Research Center for Physical Sciences at the Microscale and School of Physical Sciences, University of Science and Technology of China, Hefei, 230026, China*

[2]*Shanghai Research Center for Quantum Science and CAS Center for Excellence in Quantum Information and Quantum Physics, University of Science and Technology of China, Shanghai, 201315, China*

[3]*Hefei National Laboratory, University of Science and Technology of China, Hefei, 230026, China*

[4]*Xi'an Institute of Optics and Precision Mechanics of CAS, Xi'an 710119, China*

[5]*Center for Theoretical Physics, MIT, Cambridge, Massachusetts 02139, USA*

[6]*T. D. Lee Institute, Shanghai Jiao Tong University, Shanghai, 200240, China*

[7]*Wilczek Quantum Center, School of Physics and Astronomy, Shanghai Jiao Tong University, Shanghai, 200240, China*

[8]*Department of Physics, Stockholm University, Stockholm, SE-106 91, Sweden*

[9]*Department of Physics, Arizona State University, Tempe, Arizona 85287, USA*

Contents

A. Data acquisition simulation

To gain further insight into the mechanism of active intensity interferometry, we perform numerical simulations of data acquisition. As shown in Fig. S1, the simulated and experimental data acquisition processes are indicated as orange and purple arrows, respectively. To simulate the single-shot measurement of $c_{ab}^{(2)}$, a target (Fig. S1(a)) is first transformed into the Fourier domain to achieve its normalized Fourier magnitude (Fig. S1(c)). Then, the sparse Fourier magnitude $|f(\mathbf{k}_a - \mathbf{k}_b)|$ is sampled corresponding to our real experimental baselines. Finally, the single-shot measurement of $c_{ab}^{(2)}$ can be simulated from Fig. S1(d) using the simulation method detailed in Sec. H. The target (Fig. S1(a)) can also convert to a single-shot measurement of $c_{ab}^{(2)}$ under different baselines (Fig. S1(e)) via real outdoor experiment (Fig. S1(b)).

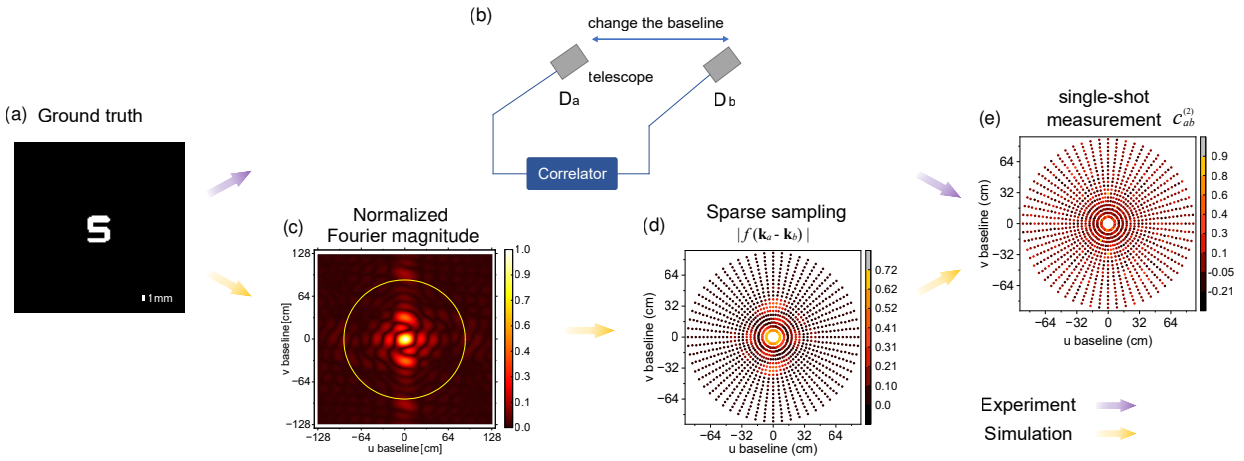

FIG. S1: **The flow chart for single-shot data acquisition with both experiment and simulation.** In the experiment module, the ground truth target (a) is observed by our intensity interferometer performing a single-shot measurement of $c_{ab}^{(2)}$ under different baselines, denoted as (e). In the simulation module, to simulate (e), the target (a) first undergoes a normalized Fourier transform, yielding its normalized Fourier magnitude (c). The yellow circle in (c) denotes the spatial frequency upper limit of the current experimental setup. Then, the sparse Fourier magnitude (d) is sampled corresponding to the real experimental baselines. Finally, the single-shot measurement of $c_{ab}^{(2)}$ (e) is simulated from (d) using the simulation method detailed in Sec. H. Scale bar: 1 mm ((a)).

B. Image Reconstruction

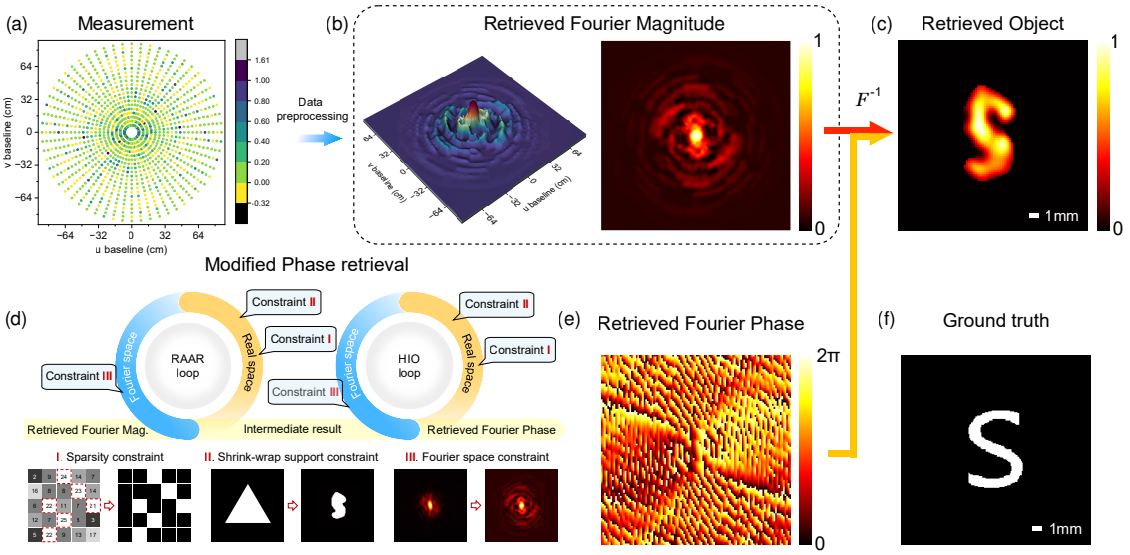

FIG. S2: **Image reconstruction.** (a) Raw measurement of the intensity correlation function $c_{ab}^{(2)}$ of the letter 'S'. (b) Fourier magnitude derived from elaborated data preprocessing. (c) The final reconstructed image obtained through the inverse Fourier transform, synthesizing the Fourier magnitude (b) with the retrieved Fourier phase (e). (d) The flowchart of our modified phase retrieval algorithm. The retrieved Fourier magnitude (b) is used as input and alternately projected and reflected in the Fourier and real domains using a cascaded RAAR and HIO strategy with multiple constraints. (e) Retrieved Fourier phase. (f) Ground truth image of the letter 'S' target. Scale bar: 1 mm ((c), (f)).

An intensity interferometer does not provide an image directly, but rather an intensity correlation function proportional to the squared-magnitude of the Fourier transform of the source brightness [1, 2]. To recover an image, the phase of the Fourier transform must be determined in addition to its magnitude [3–5]. As depicted in Fig. S2, the process of image reconstruction is primarily divided into two stages: data preprocessing and phase retrieval. During the data preprocessing stage, the $c_{ab}^{(2)}$ raw data undergoes a series of specified computational operations to extract the Fourier magnitude of the target. In the subsequent phase retrieval stage, an modified iterative algorithm is employed, using the previously obtained Fourier magnitude as input, to derive the corresponding Fourier phase. Ultimately, the target image is reconstructed by combining the Fourier magnitude and phase,

followed by an inverse Fourier transform. The following subsections outline our proposed data preprocessing and phase retrieval algorithms in detail.

i. Data preprocessing

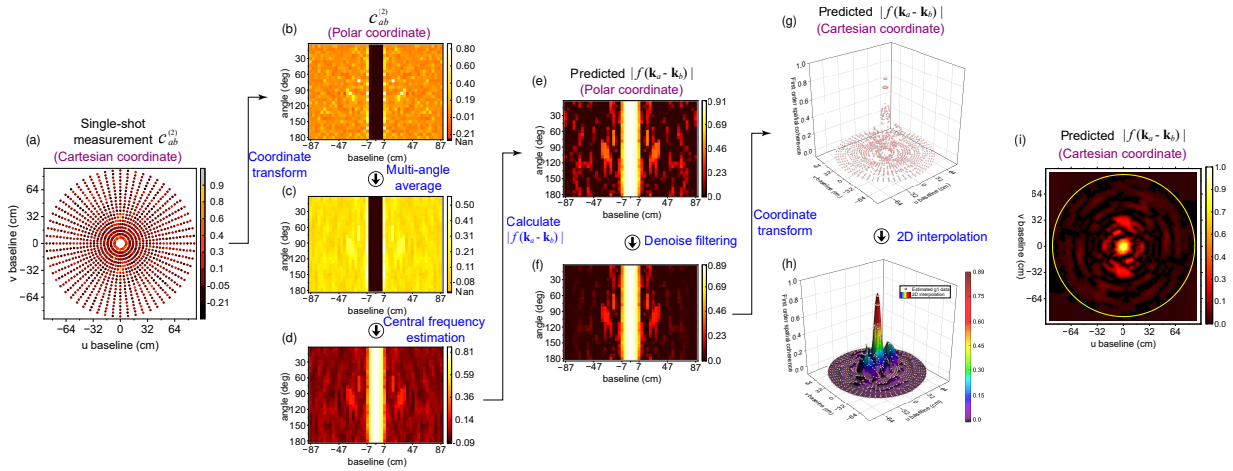

FIG. S3: **Data preprocessing.** (a) Raw measurement of $c_{ab}^{(2)}$ in Cartesian coordinate. (b) Raw measurement of $c_{ab}^{(2)}$ in Polar coordinate, derived through central symmetric averaging and subsequent coordinate transformation of (a). (b) is averaged with five adjacent angles to generate (c), which is then subjected to row-by-row 1-D interpolation to yield the central frequency estimation (d). (e) Fourier magnitude $|f(\mathbf{k}_a - \mathbf{k}_b)|$ calculated from (d). A Ram-Lak filter is applied in Fourier space to eliminate high-frequency oscillation noise, yielding the predicted $|f(\mathbf{k}_a - \mathbf{k}_b)|$ in (f). This result is transformed into Cartesian coordinates, producing (g), which is then 2-D interpolated to obtain the final predicted Fourier magnitude (h). (i) Top view of (h) with the yellow circle representing the maximum baseline region.

In Fig. S2, the data preprocessing steps that transition the data from Fig. S2(a) to Fig. S2(b) are elaborated in detail in Fig. S3. According to our experimental setup, a total of $60 \times 21 = 1260$ coincidence count sets are gathered, and the corresponding Fourier (u, v) coverage is depicted in Fig. S3(a). The interferometric sampling remains very sparse (for the 1260 experimental data points fall in 512×512 grids, leading to a 0.48% sampling ratio), and the central crucial low-frequency region (frequency components lie under the 0.07 m circle) is not measured due to the physical limitations of the distance between two

telescopes. Furthermore, extracting the target Fourier magnitude $|f(\mathbf{k}_a - \mathbf{k}_b)|$ from $\langle c_{ab}^{(2)} \rangle_e$ makes the model nonlinearity and noise sensitive to near-zero values caused by the square root operation.

To address the above issues, the raw measurement of $c_{ab}^{(2)}$ (Fig. S3(a)) is central symmetric averaged and converted into Polar coordinates (Fig. S3(b)). The adjacent five angle average is employed (Fig. S3(c)) to make the data much approach to $\langle c_{ab}^{(2)} \rangle_e$. Since our experimental setup is unable to capture the frequency range within 7 cm of the spectrum center. Interpolation points located at the position [-4 -2 0 2 4] (unit: cm) of the center null part are selected for the low-frequency component estimation. The central low frequencies are predicted by summing and averaging after 1-D cubic spline interpolation for each angle (Fig. S3(d)). The predicted target Fourier magnitude $|f(\mathbf{k}_a - \mathbf{k}_b)|$ (Fig. S3(e)) is calculated from $\langle c_{ab}^{(2)} \rangle_e$ ($c_0 = 0.06$ in main text Fig. 4 and 0.15 in Fig. S4) and then smoothed by a Ram-Lak filter [6] to remove high-frequency oscillations (Fig. S3(f)). The filtered data are transformed into Cartesian coordinates (Fig. S3(g)) and interpolated in two dimensions via MATLAB griddata function based on 'v4' method to fill the voids in the sparse sampled spatial frequencies to obtain the final predicted target Fourier magnitude (Fig. S3(h), (i)). The resulting Fourier magnitude with size of $N \times N$ is zero-padded to $2N \times 2N$, and a two dimensional separable Hanning window is applied before entering the modified phase retrieval algorithm.

ii. Phase Retrieval

As the next key ingredient in the reconstruction process, phase retrieval is designed to reconstruct an image from its Fourier magnitude. Despite rapid developments in the field of phase retrieval, robustly recovering the missing Fourier phase component from active intensity interferometry data remains a significant challenge. This complexity arises from various noise factors, including urban environmental disturbances and imperfections in pseudo-thermal light sources as well as the aforementioned Fourier space sparse sampling and model nonlinearity. To address this highly ill-posed phase retrieval problem, we employ nonconvex optimization techniques, drawing inspiration from alternating projections and reflection schemes [3, 7–9]. Specifically, apart from normalization factors, we denote the target with reflectivity $\rho(\mathbf{r})$, where $\mathbf{r}$ is the coordinates in the object (or real) space, and the

corresponding Fourier Transform $\tilde{\rho}(\mathbf{k}) = F(\rho(\mathbf{r}))$, with $\mathbf{k}$ representing the coordinate in the Fourier (or Reciprocal) space. Four operators linking two sets $\mathbf{S}$ (support) and $\mathbf{M}$ (modulus) are introduced. Given a support set $\mathbf{S}$, the support projection operator $\mathbf{P_S}$ involves setting to 0 the components outside the support while leaving the rest of the values unchanged:

$$\mathbf{P_S}(\rho(\mathbf{r})) = \begin{cases} \rho(\mathbf{r}), & \text{if } \mathbf{r} \in \mathbf{S}, \\ 0, & \text{otherwise.} \end{cases} \tag{S1}$$

The modulus projector $\mathbf{P_M}$ sets the modulus to the retrieved Fourier magnitude $m(\mathbf{k})$, and leaving the phase $\varphi(\mathbf{k})$ unchanged:

$$\mathbf{P_M}(\tilde{\rho}(\mathbf{k})) = \mathbf{P_M}(|\tilde{\rho}(\mathbf{k})|e^{i\varphi(\mathbf{k})}) = m(\mathbf{k})e^{i\varphi(\mathbf{k})}. \tag{S2}$$

The reflection operators $\mathbf{R_S} = 2\mathbf{P_S} - \mathbf{I}$ and $\mathbf{R_M} = 2\mathbf{P_M} - \mathbf{I}$ apply the same step as the projector but move twice as far, where I means the identity operator.

The phase retrieval algorithm usually requires an initial input $\rho^{(0)}(\mathbf{r})$, which is a random guess. With the notation above, the HIO algorithm can be formulated as [9]

$$\rho^{(n+1)}(\mathbf{r}) = \left[\mathbf{P_S}\mathbf{P_M} + \mathbf{P_{\underline{S}}}\left(\mathbf{I} - \beta\mathbf{P_M}\right)\right]\rho^{(n)}(\mathbf{r}), \tag{S3}$$

where $\rho^{(n)}(\mathbf{r})$ is the output after n steps of iteration, $\mathbf{P_{\underline{S}}} = (\mathbf{I} - \mathbf{P_S})$ denotes the complement of the projector $\mathbf{P_S}$ and the $\beta(0 < \beta < 1)$ here and below means a negative feedback parameter. Empirically, small β produces better stability while large β is better for escaping local minima [4]. The algorithm usually works well when β is between 0.5 and 1. In all experiments and simulations, the β is set to 0.8. Similarly, the RAAR algorithm can be written as

$$\rho^{(n+1)}(\mathbf{r}) = \left[\frac{1}{2}\beta\left(\mathbf{R_S}\mathbf{R_M} + \mathbf{I}\right) + (1-\beta)\mathbf{P_M}\right]\rho^{(n)}(\mathbf{r}). \tag{S4}$$

For better imaging performance, a combination of two different phase retrieval algorithms can improve image quality, such as HIO + ER [10]. In our scheme, we use a combination of RAAR (60 iterations) and HIO (one iteration) algorithms, we also test other similar combinations (HIO + ER, HPR + HIO, RAAR + ER, etc.) and find this combination (RAAR + HIO) works more effective. Along with the iterations, three constraints in object domain and one constraint in Fourier domain are equipped. The first object constraint is that the object has to be real (which is not shown in Fig. S2(d)). Since $m(\mathbf{k}) = m(-\mathbf{k})$ condition

is satisfied after preprocessing, this constraint is equivalent to $\varphi(\mathbf{k}) = -\varphi(-\mathbf{k})$ and can be achieved by setting $\rho^{(0)}(\mathbf{r})$ as real. The second object constraint is the sparsity constraint, which retains the top brightness (e.g., 20 %) pixels in the image and sets the remaining to zero. The third object constraint is based on the shrink-wrap support method [11], which refines the support region $\mathbf{S}$ during the iteration. Specifically, the shrink-wrap method periodically convolves the iteration with a Gaussian kernel of width σ and then applies a threshold ϵ to smear the support; i.e., the updated support for the two-dimensional case is taken to be

$$S = \left\{ \mathbf{r} : \frac{1}{2\pi\sigma^2} \int_{\mathbb{R}^2} \rho^{(n)}(\mathbf{s}) e^{-|\mathbf{r}-\mathbf{s}|^2/2\sigma^2} d\mathbf{s} \geq \epsilon \right\}. \tag{S5}$$

The Fourier domain constraint is the magnitude constraint that using $\mathbf{P_M}$ to project the modulus to $m(\mathbf{k})$. With the iterative number increases, the exported support region will change from a loose one to a tight one, which can significantly reduce the solution space and exclude spurious solutions. It is worth emphasizing that using a non-centrosymmetric initial support estimation, such as an equilateral triangle, can speed up convergence and effectively and avoid the twin-image problem [8].

In terms of implementation, the phase retrieval algorithm is performed with MATLAB 2018b in Windows 10 running on a dual-core chip Intel Core i9-10900K and 128 GB memory. A single run of the program on a 1024×1024 pixel image retrieval (composed of 60 (RAAR) +1 (HIO) iterations) took approximately 1 s. Notably, all experimental and simulation results displayed in this article are unthresholded and without color bar adjustment.

C. Imaging performance vs. number of laser emitters.

Double slit imaging is performed to evaluate the impact of different number of laser emitters on imaging performance. The slit-to-slit separation of the double slit is ∼2 mm. The experimental results under $n = 1$, 2, 4, and 8 emitters as well as the quality performance are shown in Fig. S4(a) and (b). Simulations with the same target under $n = 1$, 2, 4, 8, 16, 32, 64 and '∞' (the ground truth Fourier domain sampling) are carried out and the corresponding results are depicted in Fig. S4(a) and (c).

Considering the randomness in the simulation, we generate 50 sets of $c_{ab}^{(2)}$ for each emission group and perform 50 trials of phase retrieval for each set of data. This process yields a

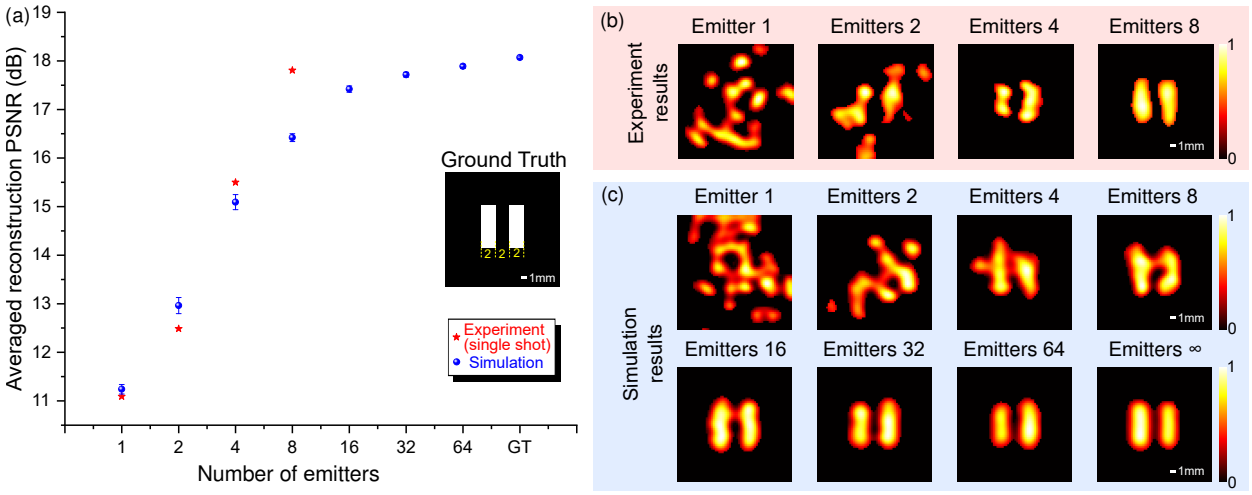

FIG. S4: **Imaging of a double slit with different number of laser emitters.** The two slits are 2 mm wide and 6 mm long, with a 4 mm center distance between the two slits. (a) Averaged reconstruction PSNR versus different number of emitters (n = 1, 2, 4, 8, 16, 32, 64 and 'GT' = Ground truth). In both simulation and experiment, the imaging quality improved as the number of emitters increased. For simulation, in each laser emission group, 50 independent sets of $c_{ab}^{(2)}$ are generated (Fig. S1) and 50 phase retrieval trials are implemented for each sets. Then, each group's average PSNR (blue dots) and its standard deviation (error bar) are calculated from $50 \times 50 = 2500$ total reconstructions. It should be noted that the results of the experiment are from single-shot measurements (red stars). (b) Experimental reconstruction results under different number of emitters (n = 1, 2, 4, 8). (c) Typical simulation reconstruction results randomly selected from each emission group. Note that the number of emitters '∞' means reconstructed image in a noise-free regime, revealing the theoretical limits of the method. Scale bars: 1 mm ((b), (c)).

total of $50 \times 50 = 2500$ reconstructions, which are used to calculate the average PSNR. The experiments and simulations embrace with each other and both indicate that at least four emitters can correctly identify the double slit. By increasing the number of emitters, the laser array illumination will be closer to thermal illumination, suppressing the speckle-like noise and thus making the double slit from indistinguishable to clearly distinguishable. The averaged error bars are fairly modest, especially when the number of emitters is greater than four. It is worth emphasizing that the experimental results are obtained by single-shot measurements.

D. Comparisons with direct telescope observations.

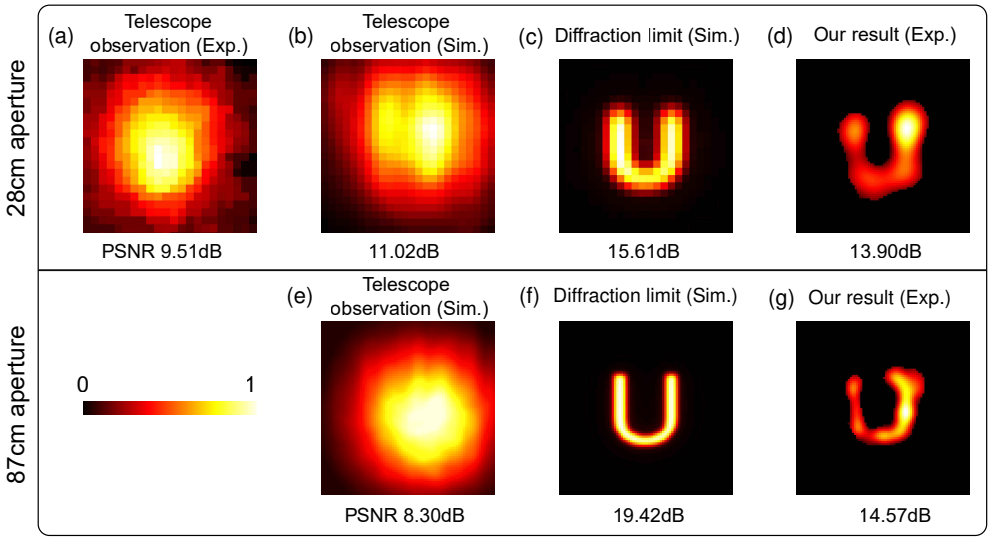

FIG. S5: **Comparisons of our proposed method with direct telescope observations.** (a) Experimental observation obtained with a $D = 28$ cm, $f = 2.8$ m Cassegrain telescope. (b) Simulated telescope observation with a $D = 28$ cm telescope under the atmospheric turbulence condition with Fried parameter $r_0 = 5$ cm. (c) Diffraction limit result of a 28 cm telescope. (d) Our reconstruction result under a baseline range of 7 cm to 27 cm. (e) Simulated observations from a $D = 87$ cm telescope with a focal length $f = 8.7$ m. (f) Diffraction limit result of a 87 cm telescope. (g) Our reconstruction result under a baseline range of 7 cm to 27 cm. Sim. and Exp. denote simulation and experiment, respectively.

To demonstrate the synthetic aperture imaging capability of our setup, we perform further comparisons with direct telescope observations of letter 'U' target with equivalent apertures. As shown in Fig. S5, the comparisons are divided into two groups according to the aperture size: 28 cm and 87 cm. For an easily obtained 28 cm aperture telescope, in addition to the experimental photography shown in Fig. S5(a), we also simulate the imaging result under the atmospheric turbulence condition with Fried parameter $r_0 = 5$ cm, as depicted in Fig. S5(b). Fig. S5(c) shows a simulation of diffraction-limited imaging for a 28 cm aperture. Our imaging results, utilizing experimental data with a baseline range of 7cm to 27cm and reconstructed using the proposed algorithm, are presented in Fig. S5(d). For the

case of 87 cm aperture, Fig. S5(e)-(g) demonstrates the results obtained by the corresponding approaches, but does not include experimental photography because we do not have access to such a large aperture telescope.

From these comparisons one can observe, despite some minor distortions, our imaging results are on par with the diffraction-limited observations. These distortions, caused by noise, are expected to diminish with advancements in future experiments and algorithms. Furthermore, unlike direct observations with large aperture telescopes, which are increasingly susceptible to atmospheric turbulence, active intensity interferometry imaging effectively circumvents this issue.

The simulation parameters employed include an f/D ratio of 10 (where f represents the focal length and D denotes the aperture size) in both 28 cm and 87 cm cases. The imaging condition mimics outdoor experiments, with the same imaging distance (1.36 km) and target size. The camera pixel sizes in all simulations are set as 3.76 μm, matching the telescope photography in Fig. S5(a). Turbulence simulations are based on the phase screen model described in [12], performed by the python 'MegaScreen' package. It's worth noting that all simulations are conducted without considering optical aberrations; therefore, actual imaging results may vary and could be less optimal compared to the simulations.

E. Different number of emitters vs acquisition frames.

In the current experimental setup, the incoherent source is modeled by a collection of emitters. Measuring the intensity correlation function $c_{ab}^{(2)}$ with pseudothermal light inevitably leads to speckle-like noise due to interference of the signal with scattered light. Except for increasing the number of emitters, averaging the numerous acquisition frames of $c_{ab}^{(2)}$ (multiple parallel measurements) can also suppress the speckle-like noise, yielding imaging quality improvement. Two shapes of targets are tested and the reconstruction results with different number of emitters and acquisition frames from numerical simulation are presented in Fig. S6. Both results show that increasing the number of laser emitters improves image quality more than increasing the acquisition frames, indicating that the thermal properties of the light source are more essential to imaging performance. Nonetheless, in the case of restricted number of emitters, imaging quality can be improved by increasing the acquisition

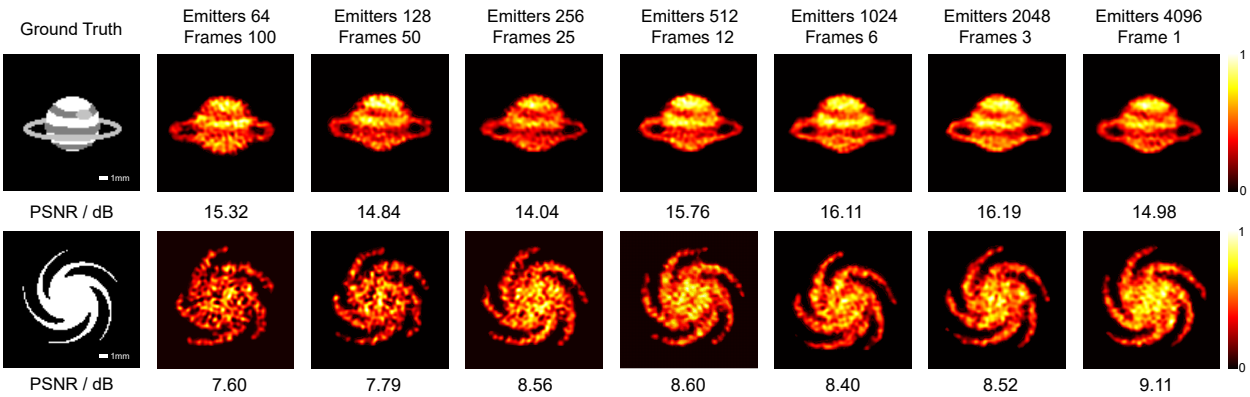

FIG. S6: **Numerical evaluations of the reconstruction with various number of emitters and acquisition frames.** Leftmost column: Ground truth of the simulated targets. Second from left: The impact of increasing the number of laser emitters while decreasing the acquisition frames but maintaining the product of the two essentially constant. The simulation parameter settings are identical to aforementioned except that the baseline shifts from 1 to 127 cm with a fixed interval of $\delta = 1$ cm. Scale bars: 1 mm (all subgraphs).

frames. To reduce the speckle-like noise, increasing the number of laser emitters n has a convergence rate of $O(1/\sqrt{n})$ and this can be further accelerated when the value of the Fourier spectrum approaches to 0 ($O(1/n)$) (Eq. (S31)). However, increasing the acquisition frames k has a convergence rate of $1/\sqrt{k}$. The variation in convergence rate causes disparities in the effectiveness of the two techniques for image quality enhancement.

F. Comparisons among different phase retrieval algorithms.

To demonstrate the superiority of the proposed phase retrieval scheme, we conducted an experimental comparison among different phase retrieval algorithms by imaging the letter 'S' in the main text (Fig. S7(f)). The letter 'S' is chosen because curve shapes contain more complex features in Fourier space. The retrieved target Fourier magnitude is noise-stained and has fainter high-frequency information, which is used as the input for all phase retrieval algorithms. The results (Fig. S7(a) to (c)) show that the Gerchberg-Saxton (GS) [3]

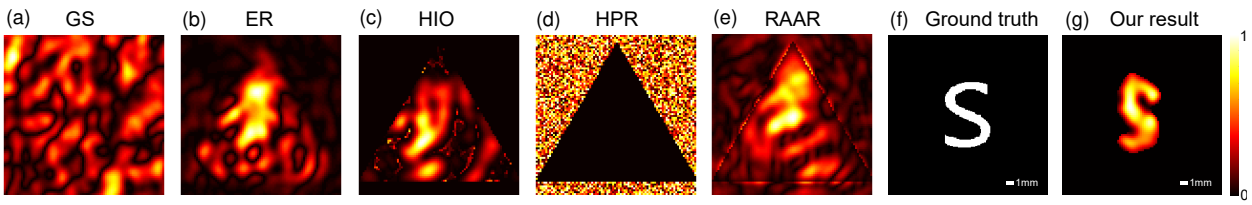

FIG. S7: **Comparisons of the reconstruction performance with different phase retrieval strategies.** (a)-(e) Reconstructions of the letter 'S' with various phase retrieval algorithms, including Gerchberg-Saxton (GS), Error Reduction (ER), Hybrid Input Output (HIO), Hybrid Projection Reflection (HPR) and Relaxed Averaged Alternating Reflectors (RAAR). Note that the iterative processes of (a)-(e) do not employ the sparse constraint and the adaptive shrink-wrap support. (f) Ground truth target. (g) Result obtained from our proposed algorithm. Scale bars: 1 mm ((f), (g)).

algorithm and its derivations such as Error Reduction (ER) [13] and Hybrid Input Output (HIO) produce poor quality images. More advanced alternating projection algorithms such as Hybrid Projection Reflection (HPR) [14] (Fig. S7(d)) and Relaxed Averaged Alternating Reflectors (RAAR) (Fig. S7(e)), are also unable to recover the target. In contrast, our reconstruction algorithm (Fig. S7(g)) outperforms the others by producing a distinguishable shape of 'S'. For the algorithms compared, the number of iterations is set to 60, a non-centrosymmetric triangle is used as the initial support, and the negative feedback parameter β for the HIO, HPR, and RAAR algorithms is fixed at 0.8.

G. Complex targets imaging via active intensity interferometry.

In this proof of concept, we have demonstrated two-dimensional synthetic aperture imaging over kilometers range with millimeters precision via active intensity interferometry. Higher-fidelity complex target reconstruction is anticipated by improving the sampling ratio on the interferometric plane and multiplying the number of baselines/telescopes. To demonstrate this, we perform imaging simulation of complex targets ('satellite' and 'UFO') with varying reflectivity levels (Fig. S8). In both simulations, the raw data is collected under a

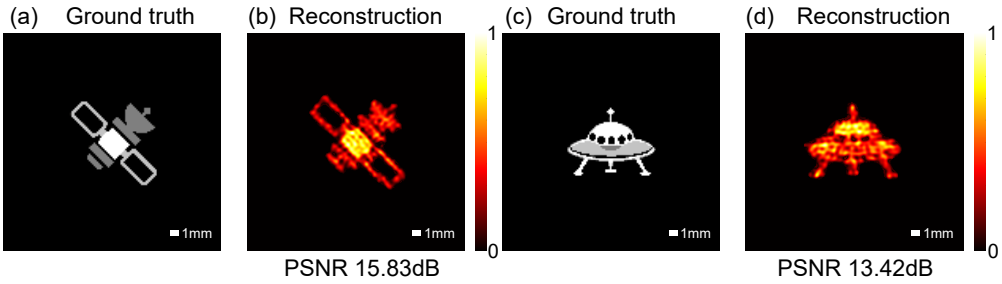

FIG. S8: **Numerical evaluations of the imaging capability of complex targets with varying levels of reflectivity.** (a)(c) Ground truth of the simulated targets. (b)(d) Reconstruction results from single-shot data acquisition. For both targets, the reconstructed irradiance is nearly identical to the true value. The baseline changes from 1 to 247 cm with a fixed interval of $\delta = 1$ cm. The remaining parameters are the same as in the experiment. Scale bars: 1 mm ((a-d)).

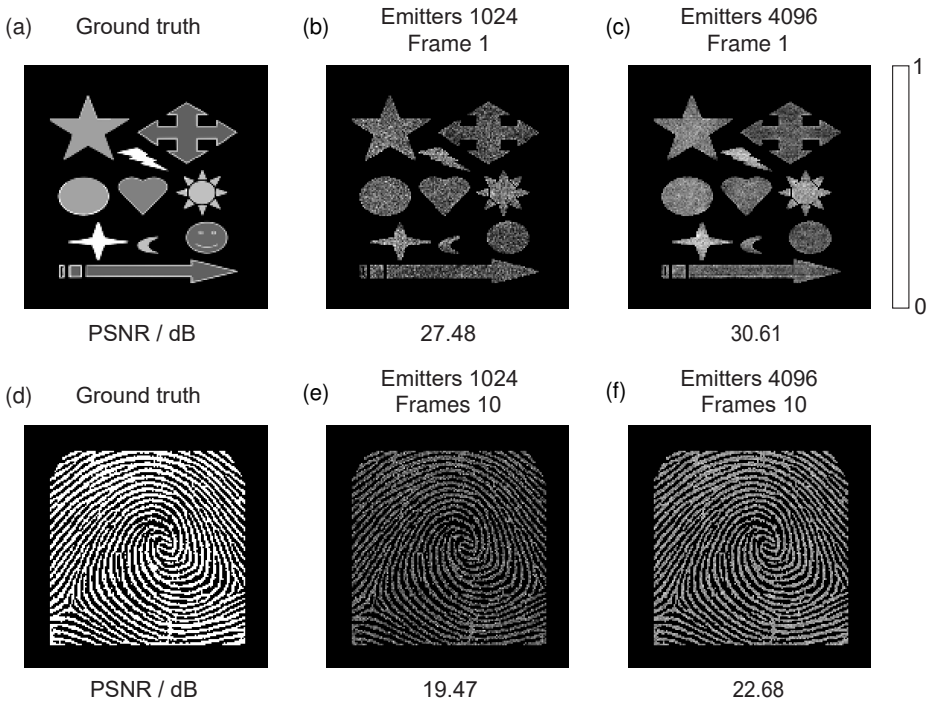

FIG. S9: **Extended complex targets imaging simulations via full Fourier plane sampling.** (a) Ground truth target of a gray-scale complex pattern. (b) Imaging result using 1024 laser emitters with a single-shot observation. (c) Imaging result using 4096 laser emitters. (d) Ground truth target of a complex "fingerprint image" target. (e)(f) Imaging results with 10 acquisition frames using 1024 and 4096 laser emitters, respectively.

maximum baseline of 247 cm with a 1 cm sampling interval.

To further validate the imaging capabilities of our proposed method for extended complex targets, two extended targets with irregular shapes, multiple regions, and fine-grained textural details are supplemented for imaging simulation. With full Fourier space sampling and sufficient number of laser emitters, active intensity interferometry can preserve sufficiently detailed information of the target despite its complex structures (Fig. S9). These results demonstrate the potential of our method for applications involving extended complex targets imaging.

H. Theory of active optical intensity interferometry.

i. Theory of multiple laser emitters with thermal nature.

We model our imaging system based on statistical optics. As shown in Fig. 1 in the main text, suppose our optical system consists of n laser emitters with angular frequency ω numbered $1 \sim n$ in the source plane, a target that is a scattering sample of a particular structure in the object plane, and two movable detectors D_a and D_b in the detection plane. Detectors D_a and D_b always use the same polarization measurement in the experiment, then we can denote the electric fields they measure on this polarization component at time t as $E_a(t)$ and $E_b(t)$, respectively. For simplicity, we only consider the case of far-field illumination and detection, that is, the distance between the target and the emitters or detectors is much greater than the Fraunhofer distance $2W^2/\lambda$, where λ is the laser wavelength and W is the maximum value among laser beam waists, detector apertures and target size.

If W is much smaller than the atmospheric coherence length, we can approximate each emitter's illumination light and its scattered light scattered by the target as an intensity- and phase-modulated plane wave. To describe these plane waves, we denote $\mathbf{k}_i$ as the wave vector from the i-th emitter to the target, and denote $\mathbf{k}_a$ and $\mathbf{k}_b$ as the wave vectors from the target to the detector D_a and D_b, respectively. Combining the above approximations and further ignoring all CW laser delays due to the time-of-flight which is much smaller

than the atmospheric coherence time, we can approximately express $E_a(t)$ and $E_b(t)$ as

$$E_{a,b}(t) = \sum_{i=1}^{n} \sqrt{I_i(t)} \mathrm{e}^{\mathrm{i}(\phi_i(t)-\omega t)} T(\mathbf{k}_i, \mathbf{k}_{a,b}) T_{a,b}(t). \tag{S6}$$

Here, $I_i(t)$ and $\phi_i(t)$ represent the intensity and phase of the plane wavefront formed at the target at time t by the illumination light from the ith emitter, $T(\mathbf{k}_{in}, \mathbf{k}_{out})$ is the target's transmission matrix [15, 16] between the $\mathbf{k}_{in}$ input field and $\mathbf{k}_{out}$ output field and $T_a(t), T_b(t)$ are propagation coefficients that describes the amplitude decay and phase change of the electric field as light propagates from the target to the detectors D_a and D_b at time t, respectively. All the $I_i(t), \phi_i(t)$ and $T_a(t), T_b(t)$ are treated as time-varying random variables which incorporate the whole process of atmospheric disturbance.

Considering that it is difficult to make a complete statistical process modeling of atmospheric disturbance, we approximate the impact of atmospheric disturbance as the following two simple statistical assumptions. The first assumption is that all the $I_i(t), \phi_i(t)$ and $T_a(t), T_b(t)$ are independent of each other. Note that this assumption clearly does not hold when the distances between different emitters or detectors are smaller than the atmospheric coherence length, so we need to avoid this in the experiment. The second assumption is that all the $\phi_i(t)$ are Gaussian random processes. Let the notation $\langle ... \rangle_t$ denote the time average over a sufficiently long time. Define $\overline{\phi_i} \equiv \langle \phi_i(t) \rangle_t$ and $\Delta\phi_i(t) \equiv \phi_i(t) - \overline{\phi_i}$, using the properties of Gaussian distribution it's easy to prove that

$$\langle \mathrm{e}^{\mathrm{i}(\phi_i(t)-\phi_j(t))} \rangle_t = \mathrm{e}^{\mathrm{i}(\overline{\phi_i}-\overline{\phi_j}) - \frac{1}{2}\langle(\Delta\phi_i(t)-\Delta\phi_j(t))^2\rangle_t}. \tag{S7}$$

In this way, if $\langle(\Delta\phi_i(t) - \Delta\phi_j(t))^2\rangle_t \gg 1$ holds for any $i \neq j$, we can further have an approximation of

$$\langle \mathrm{e}^{\mathrm{i}(\phi_i(t)-\phi_j(t))} \rangle_t = \delta_{ij} \equiv \begin{cases} 1 & i = j \\ 0 & i \neq j \end{cases}. \tag{S8}$$

This approximation is valid when the distances between different emitters are much greater than the atmospheric coherence length. In fact, the $\langle(\Delta\phi_i(t) - \Delta\phi_j(t))^2\rangle_t \approx 1$ condition can be used as a definition of atmospheric coherence length. For example, the Kolmogorov turbulence model [17, 18] expected that

$$\langle(\Delta\phi_i(t) - \Delta\phi_j(t))^2\rangle_t = 6.88(\frac{r_{ij}}{r_0})^{\frac{5}{3}}, \tag{S9}$$

where r_{ij} is the distance between the i-th emitter and the j-th emitter, r_0 is the Fried parameter, which can be used as a representation of the atmospheric coherence length.

Define $I_a(t) \equiv |E_a(t)|^2$ and $I_b(t) \equiv |E_b(t)|^2$ as the intensities measured by detectors D_a and D_b at time t, respectively. After using the above assumptions, the time-averaged intensity can be expressed as

$$\langle I_{a,b}(t)\rangle_t = \langle |E_{a,b}(t)|^2\rangle_t = \eta_{a,b}\sum_{i=1}^{n}\overline{I_i}|T(\mathbf{k}_i,\mathbf{k}_{a,b})|^2, \tag{S10}$$

where $\eta_{a,b} \equiv \langle |T_{a,b}(t)|^2\rangle_t$ and $\overline{I_i} \equiv \langle I_i(t)\rangle_t$. Define $c_i^{(2)} \equiv \langle I_i^2(t)\rangle_t/\overline{I_i}^2 - 1$, we further have the intensity correlation function

$$\begin{aligned}\langle \Delta I_a(t)\Delta I_b(t)\rangle_t &\equiv \langle I_a(t)I_b(t)\rangle_t - \langle I_a(t)\rangle_t\langle I_b(t)\rangle_t \\ &= \eta_a\eta_b[\sum_{i\neq j}\overline{I_i}\,\overline{I_j}T(\mathbf{k}_i,\mathbf{k}_a)T(\mathbf{k}_j,\mathbf{k}_b)T^*(\mathbf{k}_i,\mathbf{k}_b)T^*(\mathbf{k}_j,\mathbf{k}_a) \\ &+ \sum_{i=1}^{n} c_i^{(2)}\overline{I_i}^2|T(\mathbf{k}_i,\mathbf{k}_a)|^2|T(\mathbf{k}_i,\mathbf{k}_b)|^2].\end{aligned} \tag{S11}$$

It can be seen that for a particular target, both the time-averaged intensity and the intensity correlation function have a particular value determined by the transmission matrix $T(\mathbf{k}_{in},\mathbf{k}_{out})$ of the scattering sample. Now we consider an ensemble of scattering samples with the same geometric surface but different internal microstructure. The fully developed speckle model proposed by Goodman et al. predicts that if the sample surface is sufficiently rough compared to the wavelength of light, for each $(\mathbf{k}_{in},\mathbf{k}_{out})$ pair, the transmission coefficient $T(\mathbf{k}_{in},\mathbf{k}_{out})$ behaves as a circular complex Gaussian random variable in the ensemble [19].

We next demonstrate that this statistical property of the transmission matrix is the key factor causing speckle-like noise in the experimental data. Let the notation $\langle ...\rangle_e$ denote the ensemble average, and the notation $\langle ...\rangle_{t,e} \equiv \langle\langle ...\rangle_t\rangle_e$ denote the ensemble average of a time average quantity. Using the moment theorem [20] for complex Gaussian random variables, we have the ensemble-averaged intensity correlation function

$$\begin{aligned}\langle \Delta I_a(t)\Delta I_b(t)\rangle_{t,e} &= \eta_a\eta_b[\sum_{i\neq j}\overline{I_i}\,\overline{I_j}\langle T(\mathbf{k}_i,\mathbf{k}_a)T^*(\mathbf{k}_i,\mathbf{k}_b)\rangle_e\langle T(\mathbf{k}_j,\mathbf{k}_b)T^*(\mathbf{k}_j,\mathbf{k}_a)\rangle_e \\ &+ \sum_{i\neq j}\overline{I_i}\,\overline{I_j}\langle T(\mathbf{k}_i,\mathbf{k}_a)T^*(\mathbf{k}_j,\mathbf{k}_a)\rangle_e\langle T(\mathbf{k}_j,\mathbf{k}_b)T^*(\mathbf{k}_i,\mathbf{k}_b)\rangle_e \\ &+ \sum_{i=1}^{n} c_i^{(2)}\overline{I_i}^2(\langle |T(\mathbf{k}_i,\mathbf{k}_a)|^2\rangle_e\langle |T(\mathbf{k}_i,\mathbf{k}_b)|^2\rangle_e + |\langle T(\mathbf{k}_i,\mathbf{k}_a)T^*(\mathbf{k}_i,\mathbf{k}_b)\rangle_e|^2)].\end{aligned} \tag{S12}$$

To further obtain an explicit expression of the above formula, we need to study the coherence function of the form $\langle T(\mathbf{k}_{in1},\mathbf{k}_{out1})T^*(\mathbf{k}_{in2},\mathbf{k}_{out2})\rangle_e$, where $\mathbf{k}_{in1} = \mathbf{k}_{in2}$ or $\mathbf{k}_{out1} =$

$\mathbf{k}_{out2}$. For the first case, the classical coherence theory based on the van Cittert-Zernike theorem gives [21]

$$\langle T(\mathbf{k}_{in},\mathbf{k}_{out1})T^{*}(\mathbf{k}_{in},\mathbf{k}_{out2})\rangle_{e} \propto \int \rho(\mathbf{r})\mathrm{e}^{-\mathrm{i}(\mathbf{k}_{out1}-\mathbf{k}_{out2}).\mathbf{r}}\mathrm{d}\mathbf{r}, \tag{S13}$$

which is the Fourier transform of the intensity distribution on the output surface of the target. So let

$$\langle T(\mathbf{k}_{in},\mathbf{k}_{out1})T^{*}(\mathbf{k}_{in},\mathbf{k}_{out2})\rangle_{e} = \eta f(\mathbf{k}_{out1}-\mathbf{k}_{out2}), \tag{S14}$$

where η is a real constant and f is the normalized Fourier function, that is,

$$f(\Delta\mathbf{k}) = \frac{\int \rho(\mathbf{r})\mathrm{e}^{-\mathrm{i}\Delta\mathbf{k}.\mathbf{r}}\mathrm{d}\mathbf{r}}{\int \rho(\mathbf{r})\mathrm{d}\mathbf{r}}. \tag{S15}$$

For the second case, we assume that

$$\langle T(\mathbf{k}_{in1},\mathbf{k}_{out})T^{*}(\mathbf{k}_{in2},\mathbf{k}_{out})\rangle_{e} = \eta h(\mathbf{k}_{in1}-\mathbf{k}_{in2}), \tag{S16}$$

where h is a function that satisfies $h(0) = f(0) = 1$. For surface scattering, classical coherence theory simply predicts $h = f$, but for volume scattering, the physical mechanism here is much more complicated. Some modern studies on speckle have found that the function h is related to the optical memory effect. Both theory [22] and experiment [23] show that h will decay to 0 when $|\mathbf{k}_i - \mathbf{k}_j|$ is large, and we will not discuss the relevant details here. Substituting Eq. (S14) and Eq. (S16) into Eq. (S10) and Eq. (S12), we obtain

$$\langle I_{a,b}(t)\rangle_{t,e} = \eta_{a,b}\,\eta \sum_{i=1}^{n} \overline{I_i} \tag{S17}$$

and

$$\begin{aligned}\langle \Delta I_a(t)\Delta I_b(t)\rangle_{t,e} = \eta_a\eta_b\,\eta^2[&\sum_{i=1}^{n} c_i^{(2)}\overline{I_i}^{2} + \sum_{i\neq j}\overline{I_i}\,\overline{I_j}|h(\mathbf{k}_i-\mathbf{k}_j)|^2 \\ &+ (\sum_{i=1}^{n} c_i^{(2)}\overline{I_i}^{2} + \sum_{i\neq j}\overline{I_i}\,\overline{I_j})|f(\mathbf{k}_a-\mathbf{k}_b)|^2],\end{aligned} \tag{S18}$$

respectively. In our experiment, the quantity we measure is the normalized intensity correlation function $c_{ab}^{(2)}$, which is defined as

$$c_{ab}^{(2)} \equiv \frac{\langle \Delta I_a(t)\Delta I_b(t)\rangle_t}{\langle I_a(t)\rangle_{t,e}\langle I_b(t)\rangle_{t,e}}. \tag{S19}$$

According to Eq. (S17) and Eq. (S18), the ensemble average of $c_{ab}^{(2)}$ is

$$\langle c_{ab}^{(2)}\rangle_{e} = c_0 + c_1|f(\mathbf{k}_a-\mathbf{k}_b)|^2, \tag{S20}$$

where

$$c_0 = \frac{\sum_{i=1}^{n} c_i^{(2)} \overline{I_i}^2 + \sum_{i \neq j} \overline{I_i}\,\overline{I_j} |h(\mathbf{k}_i - \mathbf{k}_j)|^2}{(\sum_{i=1}^{n} \overline{I_i})^2}, \tag{S21}$$

and

$$c_1 = \frac{\sum_{i=1}^{n} c_i^{(2)} \overline{I_i}^2 + \sum_{i \neq j} \overline{I_i}\,\overline{I_j}}{(\sum_{i=1}^{n} \overline{I_i})^2}. \tag{S22}$$

To quantify the level of speckle-like noise, we further calculate $\sigma(c_{ab}^{(2)})$, which is the standard deviation of $c_{ab}^{(2)}$, defined as

$$\sigma(c_{ab}^{(2)}) \equiv \sqrt{\langle (c_{ab}^{(2)} - \langle c_{ab}^{(2)} \rangle_e)^2 \rangle_e}. \tag{S23}$$

If the optical memory effect of the scattering sample is neglected, we can show that

$$\sigma(c_{ab}^{(2)}) = \sqrt{d_0 + d_1 |f(\mathbf{k}_a - \mathbf{k}_b)|^2 + d_2 |f(\mathbf{k}_a - \mathbf{k}_b)|^4}, \tag{S24}$$

where

$$d_0 = \frac{\sum_{i=1}^{n} 3(c_i^{(2)} \overline{I_i}^2)^2 + \sum_{i \neq j} (\overline{I_i}\,\overline{I_j})^2}{(\sum_{i=1}^{n} \overline{I_i})^4}, \tag{S25}$$

$$d_1 = \frac{\sum_{i=1}^{n} 14(c_i^{(2)} \overline{I_i}^2)^2 + \sum_{i \neq j} (12 c_i^{(2)} \overline{I_i}^3 \overline{I_j} + 2\overline{I_i}^2 \overline{I_j}^2) + \sum_{i \neq j, j \neq k, k \neq i} 2\overline{I_i}^2 \overline{I_j}\,\overline{I_k}}{(\sum_{i=1}^{n} \overline{I_i})^4}, \tag{S26}$$

and

$$d_2 = \frac{\sum_{i=1}^{n} 3(c_i^{(2)} \overline{I_i}^2)^2 + \sum_{i \neq j} (4 c_i^{(2)} \overline{I_i}^3 \overline{I_j} + 3\overline{I_i}^2 \overline{I_j}^2) + \sum_{i \neq j, j \neq k, k \neq i} 2\overline{I_i}^2 \overline{I_j}\,\overline{I_k}}{(\sum_{i=1}^{n} \overline{I_i})^4}. \tag{S27}$$

For the derivation details of the above formula, see the next subsection.

To better understand these results from a physical perspective, we consider two simplified cases. The first case is to use only one laser emitter for illumination, that is, $n = 1$, then the ensemble average and the standard deviation of $c_{ab}^{(2)}$ can be simplified as

$$\langle c_{ab}^{(2)} \rangle_e = c_1^{(2)} (1 + |f(\mathbf{k}_a - \mathbf{k}_b)|^2) \tag{S28}$$

and

$$\sigma(c_{ab}^{(2)}) = c_1^{(2)} (3 + 14|f(\mathbf{k}_a - \mathbf{k}_b)|^2 + 3|f(\mathbf{k}_a - \mathbf{k}_b)|^4)^{\frac{1}{2}}, \tag{S29}$$

respectively. In the ideal situation without atmospheric disturbance, $c_1^{(2)} = 0$, then $c_{ab}^{(2)} = \langle c_{ab}^{(2)} \rangle_e = \sigma(c_{ab}^{(2)}) = 0$ can be further obtained, which is in line with the expectation that no intensity interference signal can be detected under ideal coherent light illumination. When atmospheric disturbance can cause an autocorrelation coefficient $c_1^{(2)}$ that cannot be ignored,

an intensity interference signal proportional to $c_1^{(2)}$ on average can actually be measured. However, since $\sigma(c_{ab}^{(2)})$ is also proportional to $c_1^{(2)}$, the level of speckle-like noise is almost the same as the signal (easy to prove that $\sqrt{3} < \sigma(c_{ab}^{(2)})/\langle c_{ab}^{(2)}\rangle_e < \sqrt{5}$), resulting in a very low SNR.

The second case is when there is more than one emitter but all emitters have identical properties and the optical memory effect of the scattering sample is neglected. We assume $\overline{I_1} = \overline{I_2} = ... = \overline{I_n}$ and $c_1^{(2)} = c_2^{(2)} = ... = c_n^{(2)} = c$ is an autocorrelation coefficient, then we have the expressions

$$\langle c_{ab}^{(2)}\rangle_e = \frac{c}{n} + \frac{n-1+c}{n}|f(\mathbf{k}_a - \mathbf{k}_b)|^2 \tag{S30}$$

and

$$\begin{aligned}\sigma(c_{ab}^{(2)}) = [&\frac{n-1+3c^2}{n^3} + \frac{2n^2+(12c-4)n+14c^2-12c+2}{n^3}|f(\mathbf{k}_a - \mathbf{k}_b)|^2 \\ &+ \frac{2n^2+(4c-3)n+3c^2-4c+1}{n^3}|f(\mathbf{k}_a - \mathbf{k}_b)|^4]^{\frac{1}{2}},\end{aligned} \tag{S31}$$

respectively. We can see that as the number of laser emitters n increases, $\langle c_{ab}^{(2)}\rangle_e$ will approach $|f(\mathbf{k}_a - \mathbf{k}_b)|^2$, and $\sigma(c_{ab}^{(2)})$ will decrease to 0 at a rate of $O(1/\sqrt{n})$, that is, the speckle-like noise will gradually disappear. When n approaches infinity, our theory and the classical HBT theory based on ideal thermal light sources will give consistent predictions.

ii. Detailed derivation of $\sigma(c_{ab}^{(2)})$.

To simplify the calculation of $\sigma(c_{ab}^{(2)})$, we first introduce the notation $X_1 \sim X_n$, which are defined as

$$X_i \equiv \overline{I_i} T(\mathbf{k}_i, \mathbf{k}_a) T^*(\mathbf{k}_i, \mathbf{k}_b) \ \ (\forall i \in \{1, 2, ..., n\}). \tag{S32}$$

Then $c_{ab}^{(2)}$ can be rewritten as

$$c_{ab}^{(2)} = \frac{\sum_{i\neq j} X_i X_j^* + \sum_{i=1}^n c_i^{(2)}|X_i|^2}{\eta^2(\sum_{i=1}^n \overline{I_i})^2}. \tag{S33}$$

We also introduce notations D and Cov to represent variance and covariance under ensemble statistics, that is, if X and Y are random variables, we define

$$\begin{aligned} D(X) &\equiv \langle X^2\rangle_e - \langle X\rangle_e^2, \\ Cov(X,Y) &\equiv \langle XY\rangle_e - \langle X\rangle_e \langle Y\rangle_e. \end{aligned} \tag{S34}$$

In this way, $\sigma(c_{ab}^{(2)})$ can be expressed as

$$\begin{aligned}\sigma(c_{ab}^{(2)}) &= \frac{\sqrt{D(\sum_{i\neq j} X_i X_j^* + \sum_{i=1}^n c_i^{(2)}|X_i|^2)}}{\eta^2(\sum_{i=1}^n \overline{I_i})^2} \\ &= \frac{\sqrt{D(\sum_{i\neq j} X_i X_j^*) + 2Cov(\sum_{i\neq j} X_i X_j^*, \sum_{i=1}^n c_i^{(2)}|X_i|^2) + D(\sum_{i=1}^n c_i^{(2)}|X_i|^2)}}{\eta^2(\sum_{i=1}^n \overline{I_i})^2}\end{aligned} \tag{S35}$$

Using the momentum theorem [20], we can simply prove that for any $i = 1 \sim n$, X_i has the following properties:

$$\begin{aligned}\langle X_i\rangle_e &= \eta\overline{I_i} f(\mathbf{k}_a - \mathbf{k}_b), \\ \langle X_i^2\rangle_e &= 2\eta^2\overline{I_i}^2 f^2(\mathbf{k}_a - \mathbf{k}_b), \\ \langle |X_i|^2\rangle_e &= \eta^2\overline{I_i}^2(1 + |f(\mathbf{k}_a - \mathbf{k}_b)|^2), \\ \langle X_i|X_i|^2\rangle_e &= 2\eta^3\overline{I_i}^3 f(\mathbf{k}_a - \mathbf{k}_b)(2 + |f(\mathbf{k}_a - \mathbf{k}_b)|^2), \\ \langle |X_i|^4\rangle_e &= 4\eta^4\overline{I_i}^4(1 + 4|f(\mathbf{k}_a - \mathbf{k}_b)|^2 + |f(\mathbf{k}_a - \mathbf{k}_b)|^4).\end{aligned} \tag{S36}$$

On the other hand, if the optical memory effect of the scattering sample is neglected, it means

$$\langle T(\mathbf{k}_{in1}, \mathbf{k}_{out1}) T^*(\mathbf{k}_{in2}, \mathbf{k}_{out2})\rangle_e = 0 \ \ (\forall \mathbf{k}_{in1} \neq \mathbf{k}_{in2}). \tag{S37}$$

It can be immediately proved that $X_1 \sim X_n$ are independent of each other, that is, any multivariate moment can always be decomposed into the form of the product of univariate moments, and its mathematical expression is

$$\langle \prod_{i=1}^n X_i^{\alpha_i} X_i^{*\beta_i}\rangle_e = \prod_{i=1}^n \langle X_i^{\alpha_i} X_i^{*\beta_i}\rangle_e, \tag{S38}$$

where $\alpha_1 \sim \alpha_n$ and $\beta_1 \sim \beta_n$ are any non-negative integers.

Using the above conclusions, we can do the following calculations:

$$
\begin{aligned}
D(\sum_{i\neq j} X_i X_j^*) &= \sum_{i\neq j}(D(X_i X_j^*) + Cov(X_i X_j^*, X_j X_i^*)) \\
&+ \sum_{i\neq j, j\neq k, k\neq i} Cov(X_i X_j^*, (X_i + X_j)X_k^* + X_k(X_i^* + X_j^*)) \\
&= \sum_{i\neq j} \eta^4 \overline{I_i}^2 \overline{I_j}^2 (1 + 2|f(\mathbf{k}_a - \mathbf{k}_b)|^2 + 3|f(\mathbf{k}_a - \mathbf{k}_b)|^4) \\
&+ \sum_{i\neq j, j\neq k, k\neq i} \eta^4 \overline{I_i}\,\overline{I_j}(\overline{I_i} + \overline{I_j})\overline{I_k}(|f(\mathbf{k}_a - \mathbf{k}_b)|^2 + |f(\mathbf{k}_a - \mathbf{k}_b)|^4), \\
Cov(\sum_{i\neq j} X_i X_j^*, \sum_{i=1}^{n} c_i^{(2)}|X_i|^2) &= \sum_{i\neq j} Cov(X_i X_j^*, c_i^{(2)}|X_i|^2 + c_j^{(2)}|X_j|^2) \\
&= \sum_{i\neq j} \eta^4 \overline{I_i}\,\overline{I_j}(c_i^{(2)}\overline{I_i}^2 + c_j^{(2)}\overline{I_j}^2)(3|f(\mathbf{k}_a - \mathbf{k}_b)|^2 + |f(\mathbf{k}_a - \mathbf{k}_b)|^4), \\
D(\sum_{i=1}^{n} c_i^{(2)}|X_i|^2) &= \sum_{i=1}^{n} D(c_i^{(2)}|X_i|^2) \\
&= \sum_{i=1}^{n} \eta^4 (c_i^{(2)}\overline{I_i}^2)^2 (3 + 14|f(\mathbf{k}_a - \mathbf{k}_b)|^2 + 3|f(\mathbf{k}_a - \mathbf{k}_b)|^4)
\end{aligned}
\tag{S39}
$$

Substituting them into Eq. (S35) yields the expression of $\sigma(c_{ab}^{(2)})$.

iii. Numerical simulation of $c_{ab}^{(2)}$ from $|f(\mathbf{k}_a - \mathbf{k}_b)|$.

This chapter will discuss how to numerically simulate $c_{ab}^{(2)}$ based on the aforementioned statistical optical model. For simplicity, we take all physical quantities to be dimensionless quantities, and only simulate the case where all laser emitters are symmetrically equivalent, that is, $\eta = 1$ (dimensionless), $\overline{I_1} = \overline{I_2} = ... = \overline{I_n} = 1$ (dimensionless) and $c_1^{(2)} = c_2^{(2)} = ... = c_n^{(2)} = c$ (autocorrelation coefficent). Substituting them into Eq. (S33), we have

$$
c_{ab}^{(2)} = \frac{|\sum_{i=1}^{n} X_i|^2 + (c-1)\sum_{i=1}^{n}|X_i|^2}{n^2}, \tag{S40}
$$

where $X_i = T(\mathbf{k}_i, \mathbf{k}_a)T^*(\mathbf{k}_i, \mathbf{k}_b)$ for any $i = 1 \sim n$ and all the $T(\mathbf{k}_i, \mathbf{k}_{a,b}) \sim \mathcal{CN}(0,1)$ are complex standard normal random variables. We further ignore the optical memory effect of the scattering sample, then according to the discussion in the previous chapter, all the X_i are independent random variables. In this case, $X_1 \sim X_n$ can be obtained by independently sampling the same random variable $X = c_1 c_2^*$ a total of n times, where $c_1 \sim \mathcal{CN}(0,1)$

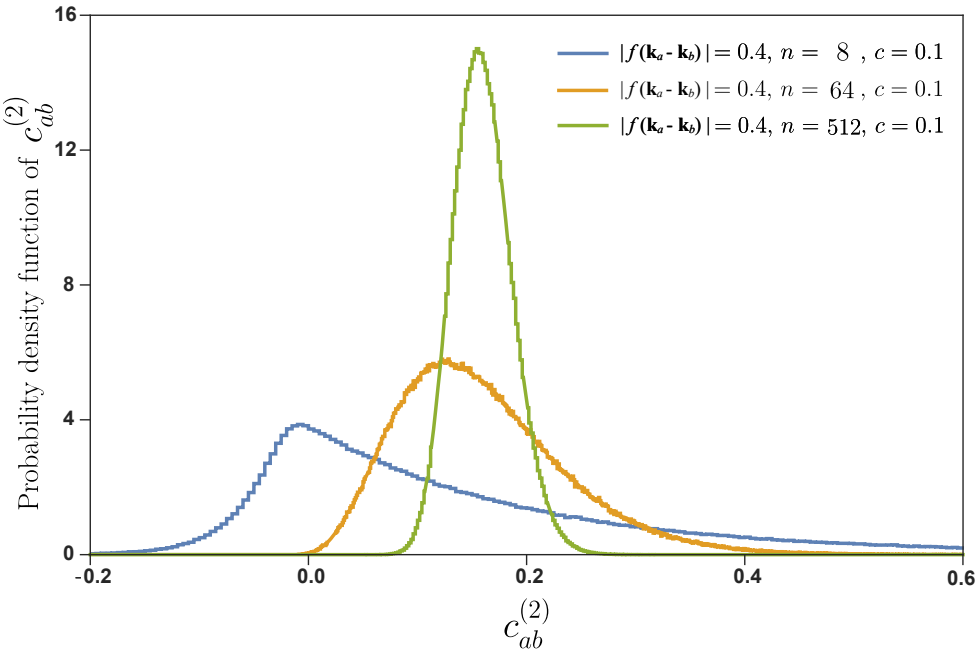

FIG. S10: **Estimation of the probability density function of $c_{ab}^{(2)}$ under multiple parallel measurements**. The blue, orange, and green lines are the numerical approximation results with different numbers of laser emitters ($n = 8, 64, 512$) but the same other input parameters ($|f(\mathbf{k}_a - \mathbf{k}_b)| = 0.4$ and $c = 0.1$). The probability density function is estimated by 10^6 repeated samples.

and $c_2 \sim \mathcal{CN}(0,1)$ satisfy $\langle c_1 c_2^* \rangle_e = f(\mathbf{k}_a - \mathbf{k}_b)$ according to Eq. (S14). Using the linear combination of circular complex Gaussian random variables still satisfying the properties of circular complex Gaussian distribution, we can equivalently sample c_1 and c_2 in the following way:

$$\begin{cases} c_1 = \sqrt{1 - |f(\mathbf{k}_a - \mathbf{k}_b)|^2} z_1 + f(\mathbf{k}_a - \mathbf{k}_b) z_2 \\ c_2 = z_2 \end{cases} . \tag{S41}$$

Here, $z_1 \sim \mathcal{CN}(0,1)$ and $z_2 \sim \mathcal{CN}(0,1)$ are independent with each other. Notably, the phase of $f(\mathbf{k}_a - \mathbf{k}_b)$ doesn't affect the final result of $c_{ab}^{(2)}$, therefore simulation from $f(\mathbf{k}_a - \mathbf{k}_b)$ and $|f(\mathbf{k}_a - \mathbf{k}_b)|$ get the same results. Putting all together, we finally formulate a numerical simulation method from $|f(\mathbf{k}_a - \mathbf{k}_b)|$ to a single-shot measurement of $c_{ab}^{(2)}$.

To simulate multiple parallel measurements of $c_{ab}^{(2)}$, one can repeat the above process independently, from which the probability density function can be estimated. Fig. S10 shows the estimated probability density function under three sets of input parameters. Qualita-

tively, when the number of laser emitters n increases while other input parameters remain unchanged, the better thermal properties makes the $c_{ab}^{(2)}$ samples distributed in a more compact interval, thus suppressing the "speckle" phenomenon, which is consistent with the theoretical derivation.

I. Estimation and Optimization of SNR in Coincidence Counting Measurement

In addition to the speckle-like noise discussed in the previous sections, for a practical intensity interferometer, the randomness of the coincidence counting measurement will also introduce noise into the intensity interference signal. For classical stellar intensity interferometers, the SNR has been shown to be estimated as [24]

$$\mathrm{SNR} \sim r\Delta\tau\sqrt{\frac{T}{\Delta t}}, \tag{S42}$$

where r is the count rate of the photon detectors (number of photons per unit time), $\Delta\tau$ is the coherence time of the light source, Δt is the time bin for coincidence counting (or the time resolution of the photon detectors) and T is the integration time. Eq. (S42) uses two important assumptions in the derivation process, one is that the time resolution of the photon detectors are much larger than the coherence time of the light source, that is, $\Delta t \gg \Delta\tau$, and the other is the Poisson noise approximation when the photon count rate is low, that is, $r\Delta\tau \ll 1$. These two assumptions are generally valid for stellar intensity interferometers whose observation targets are weak and broad-spectrum light sources.

However, for active intensity interferometry, both assumptions may not hold because of the use of pseudothermal illumination. Let us first consider only the case where the first assumption does not hold. When $\Delta t \gg \Delta\tau$, the visibility of the intensity interference signal is of $\Delta\tau/\Delta t$ magnitude, but when $\Delta t \ll \Delta\tau$, the maximum visility will be exactly 1. That is to say, when $\Delta t \ll \Delta\tau$, all coincidence events contribute to the intensity interference signal, so the SNR is approximately the square root of the total coincidence counts $r^2 T\Delta t$ over a period of time T, that is,

$$\mathrm{SNR} \sim r\sqrt{T\Delta t}. \tag{S43}$$

Combining the above two different boundary conditions, it can be found that the SNR is maximized when Δt and $\Delta\tau$ are of the same order of magnitude.

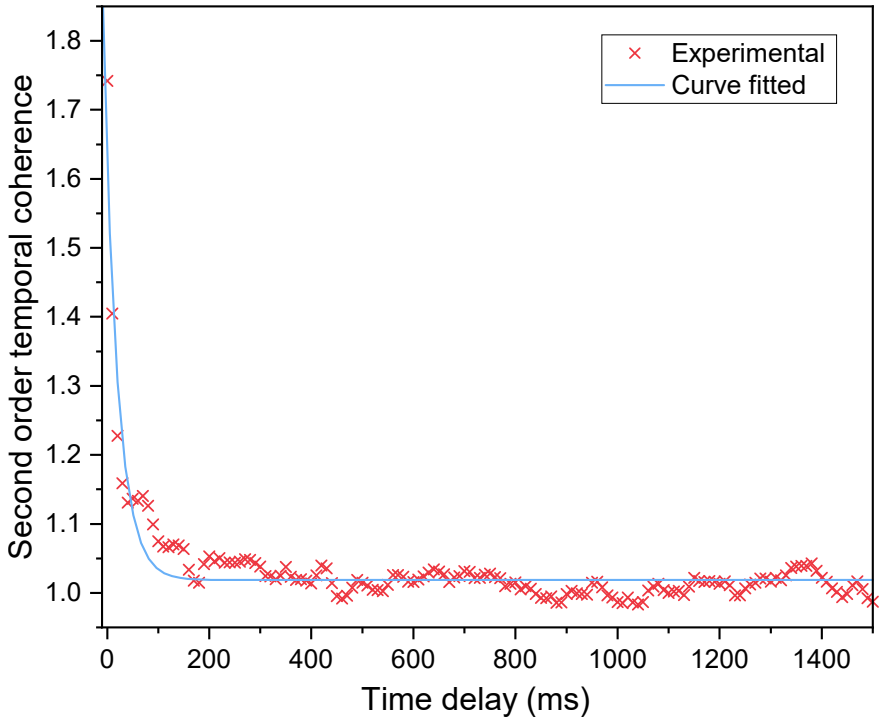

FIG. S11: **Estimation of atmospheric coherence time.** The second-order temporal coherence is calculated from the illumination intensity sequence measured by a high frame rate camera placed near the target. Using a model of second-order temporal coherence decaying exponentially with time delay, we fitted the atmospheric coherence time to approximately 27 ms.

In addition, when the count rate increases, the SNR will also increase proportionally, but it cannot be infinitely improved. When $r^2\Delta\tau\Delta t \gg 1$, on average, $r^2\Delta\tau\Delta t$ coincidence events will occur every $\Delta\tau$ time, and they are almost all correlated. That is to say, every $r^2\Delta\tau\Delta t$ consecutive coincidence events can only be approximately combined into one "effective" coincidence event. Therefore, the SNR given by Eq. (S42) or Eq. (S43) is overestimated by a factor of $r\sqrt{\Delta\tau\Delta t}$ considering that the SNR is proportional to the square root of the total coincidence rate. Ultimately, the theoretical maximum value of SNR can be expressed as

$$\max(\mathrm{SNR}) \sim \begin{cases} r\sqrt{T\Delta\tau} & \Delta t \approx \Delta\tau \text{ when } r\Delta\tau \ll 1 \\ \sqrt{\frac{T}{\Delta\tau}} & \frac{1}{r^2\Delta\tau} \ll \Delta t \ll \Delta\tau \text{ when } r\Delta\tau \gg 1 \end{cases}. \tag{S44}$$

In the experiment, we have time bin $\Delta t = 2$ ms, integration time $T = 2$ s, count rate

$r \approx 10^4$ Hz and $\Delta\tau$ is the atmospheric coherence time, which is measured to be about 27 ms as shown in Fig. S11. The value of Δt satisfies the condition for maximizing the SNR given by Eq. (S44), and it is calculated that SNR$\sim$10.

[1] P. H. Van Cittert, Die wahrscheinliche schwingungsverteilung in einer von einer lichtquelle direkt oder mittels einer linse beleuchteten ebene, Physica **1**, 201 (1934).

[2] F. Zernike, The concept of degree of coherence and its application to optical problems, Physica **5**, 785 (1938).

[3] R. W. Gerchberg, A practical algorithm for the determination of plane from image and diffraction pictures, Optik **35**, 237 (1972).

[4] J. R. Fienup, Phase retrieval algorithms: a personal tour, Applied Optics **52**, 45 (2013).

[5] Y. Shechtman, Y. C. Eldar, O. Cohen, H. N. Chapman, J. Miao, and M. Segev, Phase retrieval with application to optical imaging: a contemporary overview, IEEE signal processing magazine **32**, 87 (2015).

[6] G. Ramachandran and A. Lakshminarayanan, Three-dimensional reconstruction from radiographs and electron micrographs: application of convolutions instead of fourier transforms, Proceedings of the National Academy of Sciences **68**, 2236 (1971).

[7] J. R. Fienup, Reconstruction of an object from the modulus of its fourier transform, Optics Letters **3**, 27 (1978).

[8] J. Fienup and C. Wackerman, Phase-retrieval stagnation problems and solutions, J. Opt. Soc. Am. A **3**, 1897 (1986).

[9] S. Marchesini, Invited article: A unified evaluation of iterative projection algorithms for phase retrieval, Review of Scientific Instruments **78**, 011301 (2007).

[10] O. Katz, P. Heidmann, M. Fink, and S. Gigan, Non-invasive single-shot imaging through scattering layers and around corners via speckle correlations, Nature photonics **8**, 784 (2014).

[11] S. Marchesini, H. He, H. N. Chapman, S. P. Hau-Riege, A. Noy, M. R. Howells, U. Weierstall, and J. C. Spence, X-ray image reconstruction from a diffraction pattern alone, Physical Review B **68**, 140101 (2003).

[12] D. F. Buscher, Simulating large atmospheric phase screens using a woofer-tweeter algorithm, Optics express **24**, 23566 (2016).

[13] A. Levi and H. Stark, Image restoration by the method of generalized projections with application to restoration from magnitude, J. Opt. Soc. Am. A **1**, 932 (1984).

[14] H. H. Bauschke, P. L. Combettes, and D. R. Luke, Hybrid projection–reflection method for phase retrieval, J. Opt. Soc. Am. A **20**, 1025 (2003).

[15] C. W. Beenakker, Random-matrix theory of quantum transport, Reviews of modern physics **69**, 731 (1997).

[16] S. M. Popoff, G. Lerosey, R. Carminati, M. Fink, A. C. Boccara, and S. Gigan, Measuring the transmission matrix in optics: An approach to the study and control of light propagation in disordered media, Phys. Rev. Lett. **104**, 100601 (2010).

[17] D. L. Fried, Optical resolution through a randomly inhomogeneous medium for very long and very short exposures, JOSA **56**, 1372 (1966).

[18] K. D. Ridley, Measurements of laser phase fluctuations induced by atmospheric turbulence over 2 km and 17.5 km distances, Applied Optics **50**, 5085 (2011).

[19] J. W. Goodman, *Speckle phenomena in optics: theory and applications* (Roberts and Company Publishers, 2007).

[20] I. Reed, On a moment theorem for complex gaussian processes, IRE Transactions on Information Theory **8**, 194 (1962).

[21] J. W. Goodman, *Statistical optics* (John Wiley & Sons, 2015).

[22] S. Feng, C. Kane, P. A. Lee, and A. D. Stone, Correlations and fluctuations of coherent wave transmission through disordered media, Physical Review Letters **61**, 834 (1988).

[23] I. Freund, M. Rosenbluh, and S. Feng, Memory effects in propagation of optical waves through disordered media, Physical Review Letters **61**, 2328 (1988).

[24] V. Malvimat, O. Wucknitz, and P. Saha, Intensity interferometry with more than two detectors?, Monthly Notices of the Royal Astronomical Society **437**, 798 (2014).